Master in Quantum Science and Technology Barcelona

Master's Thesis

Cryocharacterization of an integrated superconducting cavity for suspended carbon nanotube quantum dot readout

Beñat Berasategui Miguéliz
Supervised by Víctor Román and Adrian Bachtold

Quantum NanoElectronics & NanoMechanics Group
ICFO - Institut de Ciències Fotòniques, The Barcelona Institute of Science and Technology

September 1, 2025

ICFO

Universitat de Barcelona

UAB Universitat Autònoma de Barcelona

UPC Universitat Politècnica de Catalunya BarcelonaTech

This page intentionally left blank

Cryocharacterization of an integrated superconducting cavity for suspended carbon nanotube quantum dot readout

Beñat Berasategui Miguéliz

Supervised by: Víctor Román and Adrian Bachtold

ICFO – Institut de Ciències Fotòniques, The Barcelona Institute of Science and Technology

September 1, 2025

Conventional transport measurements cannot detect charge transitions in carbon nanotube quantum dots when no net current flows, whereas existing dispersive readout approaches using separate chips suffer from parasitic capacitances and limited scalability. We developed the first fully integrated platform within our research group that capacitively couples a $\lambda/4$ niobium superconducting resonator ($f_r = 5.88$ GHz, $Q_i = 1150$, $Q_e = 1730$) directly to a suspended carbon nanotube quantum dot, enabling cryogenic measurements from 10 mK to 6 K. We successfully demonstrated dispersive readout of interdot charge transitions that are invisible to transport techniques, while also observing clear Coulomb peaks, diamonds, and stability diagrams through reflectometry measurements. This integrated approach achieves higher signal-to-noise ratios, precise control over resonance coupling, and eliminates wiring losses, establishing quantum non-demolition readout capabilities and opening new possibilities for charge qubit studies and electromechanical coupling experiments.

Keywords: Carbon nanotubes, quantum dots, Coulomb blockade, superconducting cavity, reflectometry, dispersive readout, cryogenic measurements.

Beñat Berasategui Miguéliz: benat.berasategui@icfo.eu

Acknowledgements

This thesis would not have been possible without the support and guidance of many people.

First, I want to thank Adrian for welcoming me into his research group and giving me access to all the resources I needed, from lab equipment to the knowledge of the group members. I am especially grateful to my supervisor, Víctor, who guided me through six months of research. He stayed positive even when things did not go as planned, was always patient with me, and worked very dedicatedly during the thesis writing. Special thanks to Eneko, my friend, flatmate, and lab partner, who spent so much time teaching and supporting me through all my mistakes. I also want to thank my officemates Elsa and Vignaud: Elsa for all your advice and the amazing SEM pictures that you took, which I used in this thesis, and Vignaud for his willingness to teach and provide life guidance. Thanks to Roger, whose PhD thesis became essential for my learning and who taught me so many valuable tricks for preparing aesthetic figures. Thank you to Marta for being so generous, for donating chips to me during times of scarcity, and for caring about all of us. And to Sergio, who apparently can fix anything, thank you for your patience with me and always helping out. Finally, thanks to the rest of the group —Stefan, Chris, Julie, and Eva— for all your advice and support.

I acknowledge funding from the Catalonia Quantum Academy, which supported me during this project. On a personal note, I thank my flatmates Roman, Kerman, and Eneko, who have endured living with me for a whole year and never stopped helping and encouraging me. To my friends, both those who have been there for me for years and the ones I have met in Barcelona, who have been so kind. And most importantly, to my parents, grandparents, and sister: thank you for taking such good care of me while I was writing this thesis, and for all your support over the years that got me to where I am today.

Contents

List of Acronyms

CNT	Carbon nanotube
CVD	Chemical vapor deposition
QD	Quantum dot
DQD	Double quantum dot
ICT	Interdot charge transition
RF	Radio frequency
SEM	Scanning electron microscope
SNR	Signal to noise ratio
VNA	Vector network analyzer
PCB	Printed circuit board

1 Introduction

Carbon nanotubes (CNTs) have driven major advances in nanoelectronics, sensing, and materials science because of their exceptional electronic and mechanical properties [1, 2]. In quantum technologies, CNTs enable the electrostatic definition of quantum dots and ultrastrong electromechanical coupling [3–5].

However, conventional DC transport measurements are fundamentally limited as they cannot detect coherent charge transitions inside the CNT when no net current flows [6]. A standard procedure for quantum non-demolition readout is dispersive coupling of the nanotube to a superconducting microwave resonator [7]. Typically, it requires separate chips for CNTs and resonators. Several research teams have used flip-chip and wirebond architectures [8], but parasitic capacitances and complex assembly limit yield and scalability.

A fully integrated design simplifies device assembly and enhances measurement performance. Progress in transfer-based fabrication makes suspended CNT devices compatible with superconducting materials, allowing integration on a single chip [9, 10]. Higher signal-to-noise ratios result from this method, which reaches higher frequencies where resonators couple more strongly to quantum dots. It also allows researchers to precisely engineer resonance frequency and coupling, and eliminates wiring losses. To implement this, we capacitively couple a $\lambda/4$ niobium resonator ($f_r = 5.88\,\mathrm{GHz}$, $Q_i = 1150$, $Q_e = 1730$) to a suspended CNT quantum dot and study the system from 10 mK to 6 K.

This thesis demonstrates and characterizes the performance of a superconducting resonator integrated with a suspended CNT on a single chip for the first time in our research group. To achieve this goal, Sections 2 and 3 present CNT properties and quantum dot transport. Next, Section 4 describes resonator design, Sonnet simulations, reflectometry measurements, and fitting procedures. Section 5 then demonstrates dispersive readout of interdot charge transitions. Together, this work establishes a reproducible platform for CNT-based devices for our group and facilitates future studies of charge qubits and electromechanical coupling in CNTs.

2 Carbon nanotubes

Carbon nanotubes are hollow cylindrical nanostructures composed of a single layer of carbon atoms [11]. The diameters of CNTs are in the range of a few nanometers, while their lengths can reach several millimeters or even centimeters, yielding a length-to-diameter aspect ratio exceeding 10^7. Under tension, they are two orders of magnitude stronger than steel but six times lighter [2]. Because of their remarkable mechanical properties and high electrical and thermal conductivity, carbon nanotubes are valuable in nanotechnology and materials science [12].

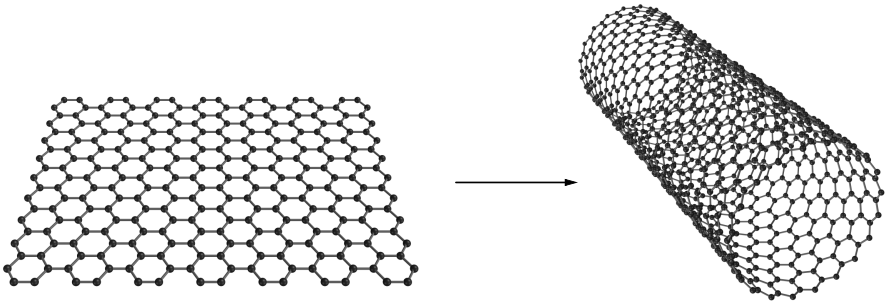

Figure 1: Carbon nanotubes can be visualized as rolled-up sheets of graphene.

CNTs, discovered by Sumio Iijima in 1991 [1], are carbon allotropes like graphene, graphite, and fullerenes. They can be visualized as rolled-up sheets of graphene[1]. In fact, the electronic properties of CNTs can be understood by examining the electronic properties of graphene [3, 11].

2.1 Electronic properties of graphene

Lattice vectors $\mathbf{a_1}$ and $\mathbf{a_2}$ define the graphene unit cell, which contains two carbon atoms separated by a distance $a = 1.42\,\text{Å}$. Each of the atoms has four electrons in the outermost atomic shell. The s, p_x, and p_y orbitals hybridize, forming three sp^2 orbitals. These orbitals create σ covalent bonds with adjacent atoms, which cause the rigidity of this material. The p_z orbitals hybridize with those of the neighboring atoms creating π bonds. Many π bonds combine to form valence (π) and conduction (π^*) bands, which determine the electronic transport properties of graphene (see Fig. 2a).

The reciprocal lattice of graphene is constructed from the reciprocal lattice vectors $\mathbf{b_1}$ and $\mathbf{b_2}$, which fulfill the relation $\mathbf{a_i} \cdot \mathbf{b_j} = 2\pi\delta_{ij}$. We use them to define the Brillouin zone: a hexagon in the k-space. The valence and conduction bands meet at the corners of this hexagon, known as the *Dirac points* K and K'. In the vicinity of these points, bands present a conical shape (Fig. 2a), and the dispersion relation between energy and momentum can be linearly approximated as

$$E(\mathbf{k}) \approx \pm\hbar v_F |\mathbf{k}|, \tag{1}$$

with $v_F \approx 8 \times 10^5\,\text{m}\,\text{s}^{-1}$ the Fermi velocity [14].

The K and K' points are inequivalent and they give rise to a 2-fold degeneracy known as the valley degree of freedom [11]. A four-fold degeneracy emerges from combining valley and spin degrees of freedom. This degeneracy is experimentally accessible via transport measurements in ultra-clean CNTs, as we will show in Section 3.

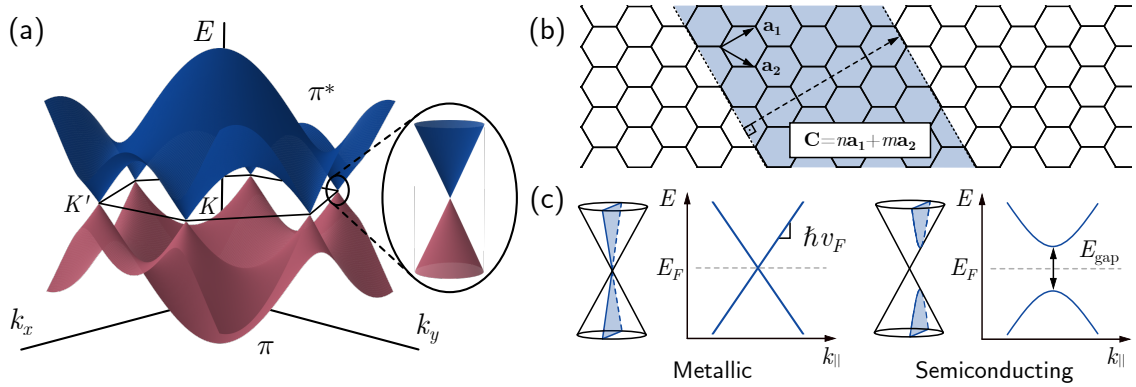

Figure 2: (a) Band structure of graphene. The valence and conduction bands meet at the K and K' points, known as Dirac points. The dispersion relation can be approximated linearly in the vicinity of these points, yielding a conical shape. Adapted from Refs. [14, 15] (b) The chiral vector $\mathbf{C}$ defines the circumference of the nanotube, and it is perpendicular to the nanotube axis. (c) The band structure of the nanotube depends on the intersection between quantization lines and Dirac cones. From Ref. [11].

2.2 Zone folding approximation

A CNT can be seen as a rolled-up sheet of graphene. The rolling direction of the sheet is described by the *chiral vector* $\mathbf{C}$, which is perpendicular to the nanotube axis and defines

[1] Graphene is a two-dimensional hexagonal lattice of carbon atoms. After its isolation in 2004 by Andre Geim and Konstantin Novoselov [13], it opened the door for the field of 2D materials research.

the circumference of the nanotube (Fig. 2b).

$$\mathbf{C} = n\mathbf{a_1} + m\mathbf{a_2}, \tag{2}$$

where n and m are integers that define the *chirality* of the nanotube: CNTs can be classified as zigzag $(n, 0)$, armchair (n, n), or chiral (n, m).

The nanotubes can thus be modelled as graphene with periodic boundary conditions along the circumference. This is called the *zone folding approximation*, and it is valid when the diameter of the nanotube is much larger than the interatomic distance. As a consequence of the additional boundary conditions, the allowed wavevectors along the circumference of the nanotube are quantized [12]:

$$\psi_{\mathbf{k}}(\mathbf{r} + \mathbf{C}) = e^{i\mathbf{k}\cdot\mathbf{C}}\psi_{\mathbf{k}}(\mathbf{r}) = \psi_{\mathbf{k}}(\mathbf{r}), \tag{3}$$

which imposes the condition $\mathbf{k} \cdot \mathbf{C} = 2\pi l$, with l an integer. The resulting quantization lines determine whether the nanotube is metallic or semiconducting, depending on their intersection with the K, K' points [12]. Figure 2c shows that if the lines intersect the Dirac points the nanotube is metallic, whereas if they do not, an energy gap opens up, making the nanotube semiconducting [11]:

$$E_{\text{gap}} = \frac{4\hbar v_F}{3d} \approx \frac{0.7}{d}\text{eV nm}, \tag{4}$$

where d is the diameter of the nanotube. This yields a 175 meV band gap for typical 4 nm diameter tubes. The true value of the gap depends on additional factors, such as the tension applied to the CNT.

2.3 Device fabrication

Our devices consist of a carbon nanotube suspended between two electrodes, called source and drain. Five additional electrodes, called gates, are placed under the CNT (see Fig. 3). The distance between the source and drain is referred to as the *trench*. The gate electrodes are not galvanically connected to the CNT, but they can control the electrostatic potential due to capacitive coupling to the nanotube.

Our group has two collaborators involved in the fabrication of the devices. Dr. D. A. Czaplewski, from Argonne National Laboratory [16], helps with the design and performs the nanofabrication techniques needed to define the electrodes. The prepatterned wafers are then inspected at ICFO and sent to Chiral Nano afterwards [17]. They transfer single nanotubes, placing them over the trench. The technique is called *stapling*, and it is similar to the one described in [9, 10, 18].

The layers of the prepatterned chips are shown in Fig. 3a. The fabrication process starts with a high resistivity silicon wafer ($> 10\,\text{k}\Omega\,\text{cm}$), covered by a 292 nm thick layer of thermally grown silicon dioxide. The electrodes are made by depositing a 100 nm layer of niobium. The source and drain electrodes are made taller by evaporating 5 nm of titanium and 150 nm of palladium. Finally, etching of SiO_2 is done, resulting in gates being left on top of SiO_2 ridges. This prevents electrical shorts between adjacent electrodes [11].

The trench in our designs can vary from 500 nm to a few micrometers, and gates can be patterned down to 50 nm in width. The transferred nanotube is at a distance of 150 nm from the gates. Transfer techniques avoid the high-temperature conditions of chemical vapor deposition (CVD) growth, which was the standard method to fabricate CNTs in the past [19, 20]. CVD requires temperatures above 900 °C, making CNTs incompatible with superconducting materials. The transfer technique also allows us to preselect semiconducting CNTs before placing them.

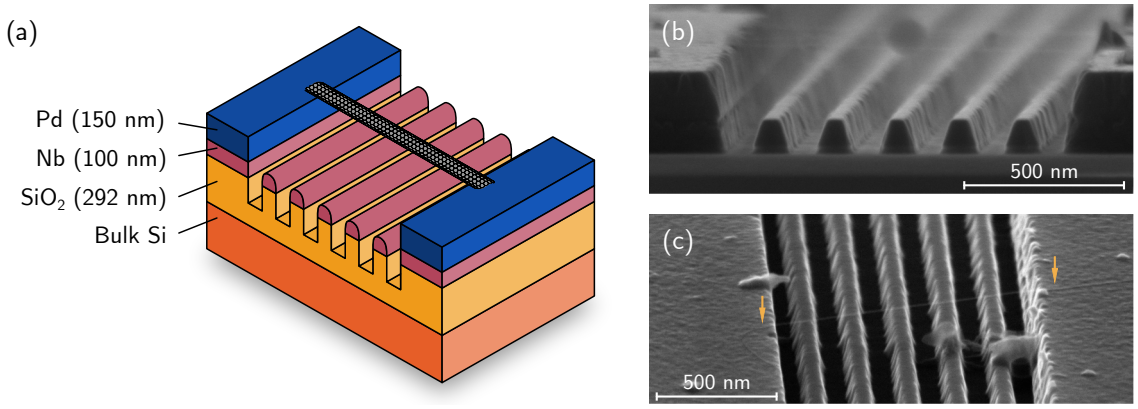

Figure 3: (a) Schematic of the layers of the device. The nanotube is stamped over a five-gate structure. The 5 nm thick titanium layer on top of niobium (not shown in the image) is used to improve the adhesion of palladium. SEM micrographs: (b) side view of the device, (c) top view of the device. Yellow arrows indicate the two ends of the nanotube.

2.4 Device characterization

We characterize devices at room temperature after receiving them at ICFO, to select the suitable ones for our experiments.

2.4.1 Air probe station

We perform the initial checks on the devices using an air probe station. This setup has two tips that can be placed on different pads of the chips using a micropositioner (Fig. 4a). A voltage is then applied between the two probes, and the current flowing through them is measured.

To check the presence of nanotubes, we apply a source-drain voltage V_{sd} that ramps between $-10\,\mathrm{mV}$ and $10\,\mathrm{mV}$. When there is a CNT connecting source and drain, the current increases linearly with V_{sd}, and we measure R_{sd} resistances of $10\,\mathrm{k\Omega}$ to $1\,\mathrm{M\Omega}$. If no nanotube is present, the circuit is open and hence no current flows through the tips. The same procedure is used to check for possible electric leaks between the source, drain and gate electrodes. If there is a leak, it means that the nanotube is contacting the gate, and it is not adequate for our experiments.

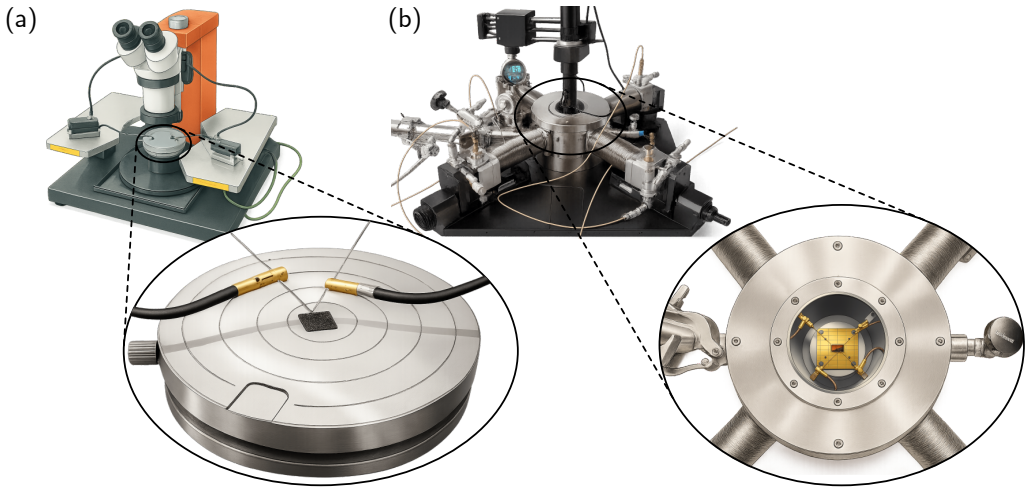

Figure 4: Illustrations of the probe stations used for room temperature characterization of the devices. (a) Air probe station. (b) Vacuum probe station.

2.4.2 Vacuum probe station

The devices are next moved to a vacuum probe station. This setup allows us to apply higher voltages to the gates, and to study the modulation of the conductance through the nanotube with the gate electrodes. The vacuum prevents air ionization. Without vacuum, high voltages would cause dielectric breakdown and damage CNTs. This station consists of a vacuum chamber with four probes that can be positioned over the pads of the chip, as Fig. 4b shows. A camera above the chamber allows us to see the chips on a screen.

We apply a source-drain voltage $V_{\mathrm{sd}} = 20\,\mathrm{mV}$, and we sweep the gate voltage V_{g} from $-3\,\mathrm{V}$ to $3\,\mathrm{V}$. The nanotube is connected in series with a $100\,\mathrm{k}\Omega$ resistance. We measure the voltage drop across this resistance, and use it to calculate the conductance $G_{\mathrm{CNT}} = 1/R_{\mathrm{CNT}}$ of the nanotube. Semiconducting nanotubes typically show a "V"-shaped conductance as a function of gate voltage (Fig. 5). This field-effect behavior is desirable for our experiments. The gate voltage shifts the Fermi level relative to valence and conduction band edges, allowing us to control the current flow through the nanotube. The current through the gate is also monitored in this setup, which allows us to detect leaks that were not visible in the air probe station.

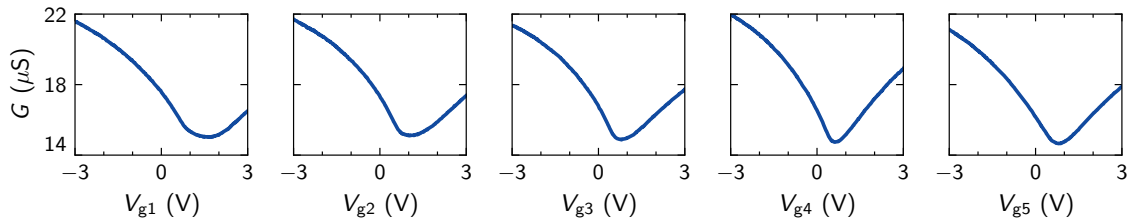

Figure 5: Five consecutive measurements of the modulation of the conductance of a suspended CNT from source to drain. We sweep each gate individually, keeping the rest grounded. Nanotubes that modulate their conductance when the gate voltage is varied are desirable for our experiments. The minimum in conductance corresponds to the band gap, which separates hole (left) and electron (right) conduction regions.

3 Transport through quantum dots

In this section, we will introduce the basic concepts of quantum dots, their transport properties and how they are used to study electron-electron interactions. We will also discuss the double quantum dot, a system that allows for the study of electronic states resembling an artificial molecule and where qubits based on the electric charge degree of freedom can be defined.

3.1 Single quantum dots

A quantum dot (QD) is an artificial 0-dimensional system that spatially confines charge carriers (electrons or holes) in three dimensions [4]. QDs are often referred to as *artificial atoms* [21], as they share some properties with natural atoms, such as discrete energy levels and the ability to confine charge carriers. However, quantum dots provide tunable energy levels and controllable electron number through external gates, which modify the electric potential. Electrons in CNTs are naturally confined to one dimension. Adding longitudinal tunnel barriers allows full quantum dots to form [3].

We study the physical properties of QDs by measuring electron transport. Two energy scales determine these properties: the charging energy E_C and the single particle level spacing ΔE [4, 22].

∗ Because of the Coulomb repulsion between electrons, adding a single electron to the

quantum dot requires a certain amount of electrostatic energy, the charging energy $E_C = e^2/C$. C is the total capacitance of the dot.

* The three-dimensional confinement creates discrete energy levels, separated by $\Delta E = hv_F/(2L)$, where L is the confinement length, *i.e.*, the size of the quantum dot.

Combining these two, the total energy needed to add a charge to the QD is given by the addition energy [11],

$$E_{add} = E_C + \Delta E. \tag{5}$$

For the number of electrons N on the dot to be a well-defined integer, the tunnel barriers must be high enough, $\hbar\Gamma \ll E_C$, where $\Gamma = \Gamma_s + \Gamma_d$ is the tunnelling rate to source and drain electrodes. In this regime, adding electrons to the QD becomes blocked until the applied voltage provides enough energy to overcome the addition energy E_{add}. This phenomenon is known as *Coulomb blockade* [23]. The two main conditions for Coulomb blockade to happen are related to the resistance and temperature of the system [22].

1. The approximate time that a charge spends on the dot is $\tau_{dot} \approx 1/\Gamma$, where $\tau_{dot} = R_t C$. R_t is the tunnel resistance and $C = C_\mathrm{s} + C_\mathrm{g} + C_\mathrm{d}$ is the total capacitance of the dot. This time is related to the charging energy E_C by the Heisenberg uncertainty principle

$$E_C \tau_{dot} \geq h, \tag{6}$$

which gives a lower bound for the tunnel resistance R_t,

$$R_t \geq \frac{h}{e^2} = R_Q. \tag{7}$$

$R_Q \approx 25.8\,\mathrm{k\Omega}$ is the quantum of resistance [20]. In CNT quantum dots this condition is achieved through gate-defined barriers.

2. The temperature of the system must be low enough to avoid thermal excitations that would allow the electrons to tunnel through the barriers. The thermal energy $k_B T$ must be smaller than the charging energy E_C,

$$k_B T \ll E_C. \tag{8}$$

If the thermal energy is also smaller than the single particle level spacing ΔE, only one energy level will contribute to electron transport. That is the reason why most experiments are done at cryogenic temperatures, in the mK to few K range.

3.1.1 Constant interaction model

For a more detailed description of the QD transport properties, we can use the constant interaction model [24]. This model allows us to describe the system as a series of lumped elements (Fig. 6a). It assumes that the capacitances are constant, *i.e.*, they do not depend on the number of electrons in the dot. The single particle energy levels are also assumed to be independent of the number of electrons in the dot. Under these assumptions, the total energy $U(N)$ of a system with N electrons is given by

$$U(N) = \frac{\left[-e\left(N - N_0\right) + C_\mathrm{g} V_\mathrm{g} + C_\mathrm{s} V_\mathrm{s} + C_\mathrm{d} V_\mathrm{d}\right]^2}{2C} + \sum_{n=1}^{N} E_n, \tag{9}$$

where $C = C_\mathrm{g} + C_\mathrm{s} + C_\mathrm{d}$ is the total capacitance of the dot, E_n are the single particle energy levels and N_0 is the charge in the dot compensating the positive background charge.

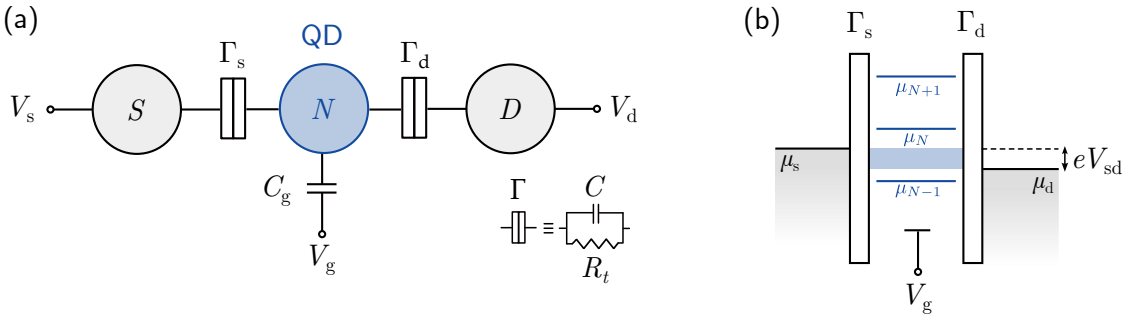

Figure 6: (a) Constant interaction model for a single quantum dot. We represent tunnel barriers as a capacitor and a resistor connected in parallel. (b) Electrochemical potential diagram of a single dot. Current can flow from source to drain when one of the energy levels is inside the bias window $\mu_s - \mu_d = -eV_{sd}$. Adapted from Ref. [11].

From Eq. (9), we can define the electrochemical potential $\mu(N)$ as the energy required to add the Nth electron to the quantum dot [3],

$$\mu(N) = U(N) - U(N-1). \tag{10}$$

Fig. 6b shows the electrochemical potential diagram of a single dot. Substituting Eq. (9) into Eq. (10), we obtain

$$\mu(N) = \frac{e^2}{C}(N - N_0 - 1/2) - \frac{e}{C}(C_g V_g + C_s V_s + C_d V_d) + E_N. \tag{11}$$

We can now calculate the addition energy E_{add} as

$$E_{add} = \mu(N+1) - \mu(N) = \frac{e^2}{C} + E_{N+1} - E_N, \tag{12}$$

which is the same as Eq. (5), where we recognize the charging energy $E_C = e^2/C$ and the single particle level spacing $\Delta E = E_{N+1} - E_N$. When two consecutive electrons are added to a degenerate level, $E_{N+1} = E_N$ and $\Delta E = 0$.

To quantify the coupling of the ith gate to the dot, *i.e.*, how much the electrochemical potential of the dot changes when the voltage on the gate is modified, we define the *lever arm* $\alpha_i = eC_i/C$ [3]. Using this definition, we can rewrite Eq. (11) in a more convenient way:

$$\mu(N) = (N - N_0 - 1/2)E_C - \sum_i \alpha_i V_i + E_N, \tag{13}$$

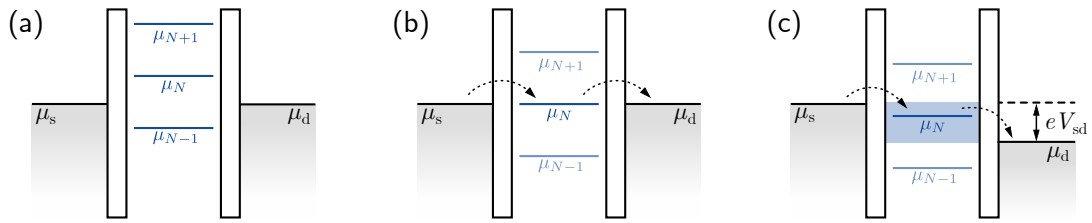

Figure 7: Energy levels of a single quantum dot. The electrochemical potential μ(N) is modified by the gate voltage V_g. The source electrochemical potential μ_s can be tuned by the source voltage V_s. We consider the drain is grounded, $V_d = 0$. Current can only flow when $\mu_s \geq \mu_N \geq \mu_d$. (a) No current flows through the dot. (b) Charge can flow through the dot sequentially. (c) At finite source bias, current can flow through the dot in a wider range of gate voltages.

3.1.2 Coulomb blockade oscillations

Consider the diagram in Fig. 6b. Γ_s and Γ_d are the tunnelling rates to the source and drain contacts, respectively. Their electrochemical potentials (μ_s and μ_d) can be modified changing the bias voltage: $\mu_s - \mu_d = -eV_{\mathrm{sd}}$, $e > 0$. Setting $V_{\mathrm{sd}} = 0\,\mathrm{V}$, the discrete levels inside the QD are given by Eq. (13). This shows that the level $\mu_N = \mu(N)$ gets lower as the gate voltage V_{g} is increased. Fig. 8 shows experimental data of Coulomb blockade oscillations in the conductance $G = dI/dV_g$ through a single QD defined in a CNT.

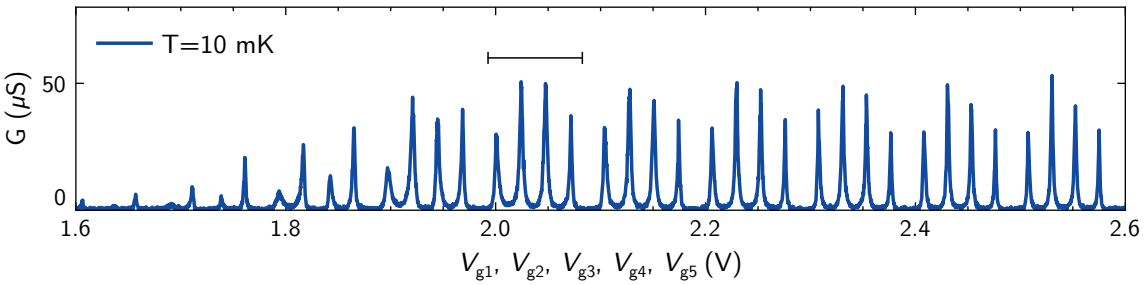

Figure 8: Experimental measurements of Coulomb blockade oscillations in the current through a single quantum dot. $V_{sd} = 0$ V and $T = 10$ mK. The black line indicates a 4-fold degenerated level. The peak spacing is $E_C/\alpha_g = 23.1 \pm 0.6$ mV, and the level spacing $E_{add}/\alpha_g = 31.6 \pm 0.3$ mV. This yields a single particle level spacing of $\Delta E/\alpha_g = 8.5 \pm 0.7$ mV.

When μ_N is misaligned with the source and drain electrochemical potentials, no current flows through the dot (Fig. 7a). However, when $\mu_s \geq \mu_N \geq \mu_d$, the electrochemical potential of the dot is resonant with the source and drain, and charge can flow through the dot sequentially (Fig. 7b). The resulting peaks in the conductance are known as *Coulomb peaks*, and they are separated by $\Delta V_{\mathrm{g}} = E_{add}/\alpha_G$. This measurement is particularly meaningful as it clearly shows the four-fold degeneracy of the CNT electronic structure that was described in Section 2.

3.1.3 Coulomb diamonds

If we now allow the source and drain electrochemical potentials to vary, we can explore another dimension of the system. For simplicity, we will consider the case where the drain is grounded. At higher source bias, $|eV_{\mathrm{sd}}| = \mu_s > \mu_N \geq \mu_d$, tunnelling is allowed in a wider range, known as the *bias window* (Fig. 7c). The map that is obtained by plotting the conductance G as a function of the gate voltage V_{g} and the source-drain voltage V_{sd} shows a series of diamond-shaped regions, the *Coulomb diamonds*. Inside them, there is no current flow. Figure 9 shows a schematic of ideal Coulomb diamonds in CNTs.

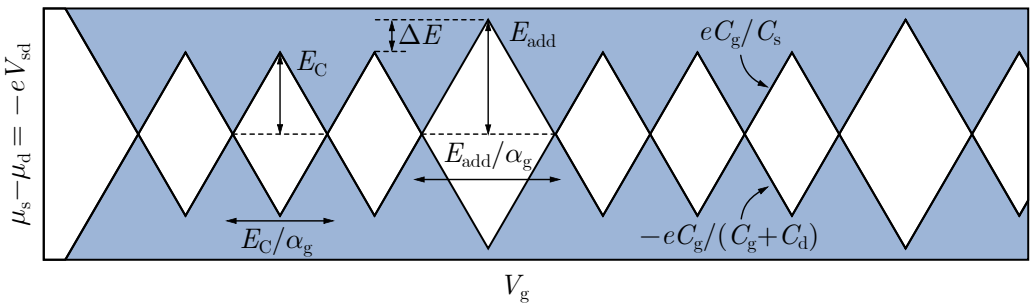

Figure 9: Coulomb diamonds are useful to retrieve many parameters of the constant interaction model. The leftmost biggest diamond corresponds to the band gap. The four-fold period of diamonds in CNTs is a consequence of spin and valley degrees of freedom. Experimental data showing this clearly four-fold degeneracy can be found in Fig. 1 from Ref. [25]. Slope equations taken from Ref. [4].

Coulomb diamonds are a useful tool to quantify the energy scales, the gate lever arms, as well as the coupling to the source and drain contacts. For instance, for the data in Fig. 8, the corresponding diamonds yield $\alpha_g = 0.21 \pm 0.02$ eV/V, $E_C = 4.8 \pm 0.5$ meV, $E_{add} = 6.6 \pm 0.6$ meV and $\Delta E = 1.8 \pm 0.2$ meV. See Appendix A for more details.

3.2 Double quantum dots

We now turn to the case of two quantum dots coupled in series, forming a double quantum dot (DQD). This system opens the possibility to study the interaction between the two dots and ultimately, to define an artificial molecule, whose two lowest energy levels define a so-called *charge qubit*.

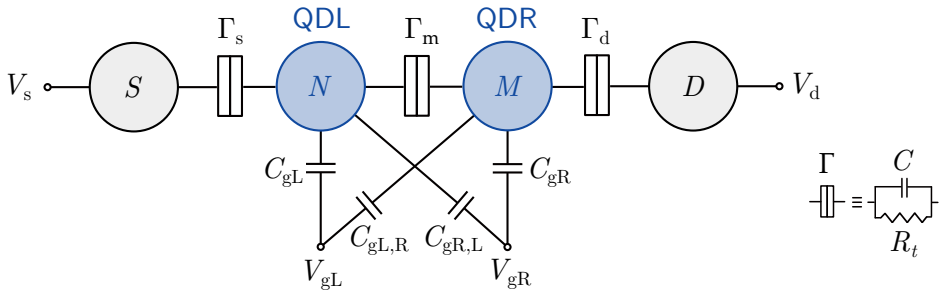

Figure 10: Constant interaction model for a double quantum dot. The left dot (QDL) contains N electrons, and the right dot (QDR) contains M electrons. The gates are named V_{gL} and V_{gR}. $C_{gL,R}$ and $C_{gR,L}$ are cross-capacitances. The barrier Γ_m determines interdot coupling.

The constant interaction model can be used to describe the DQD (Fig. 10), but in this case the calculations are more complex. For simplicity, we will not include the single particle energy levels in this discussion, and moreover, we will consider the zero bias case, $V_{sd} = 0$. Also, we will not consider any residual charge, *i.e.*, $N_0 = 0$, and we will neglect the cross-capacitances between gate i and the other dot j, $C_{gidj} = 0$.

We will follow the derivation from Ref. [6]. The total energy of the system is now dependent on the number of electrons in both dots, N and M: $U(N, M)$. Proceeding as before, we can retrieve the chemical potentials $\mu_L(N, M)$ and $\mu_R(N, M)$ of the two dots as $\mu_L(N, M) = U(N, M) - U(N-1, M)$ and $\mu_R(N, M) = U(N, M) - U(N, M-1)$. Using the expression for the total energy given in the Appendix B, Eq. (24), we can write the electrochemical potentials as

$$\mu_L(N, M) = \left(N - \frac{1}{2}\right) E_{CL} + M E_{Cm} - \frac{1}{e}\left(C_{gL} V_{gL} E_{CL} + C_{gR} V_{gR} E_{Cm}\right), \tag{14}$$

$$\mu_R(N, M) = \left(M - \frac{1}{2}\right) E_{CR} + N E_{Cm} - \frac{1}{e}\left(C_{gL} V_{gL} E_{Cm} + C_{gR} V_{gR} E_{CR}\right). \tag{15}$$

with $e > 0$. The explicit expressions of charging energies E_{CL}, E_{CR}, and E_{Cm} are given in Appendix B, Eq. (25).

3.2.1 Charge stability diagram

The charge stability diagram of a DQD is a map on which the conductance is plotted as a function of the two gate voltages V_{gL} and V_{gR}, keeping the voltages of the remaining gates fixed. The conditions for electrochemical potential alignment give rise to a honeycomb pattern. If no bias voltage is applied, $\mu_s = \mu_d = 0$. The equilibrium charges on the dots are the largest values of N and M for which $\mu_L(N, M) \leq 0$ and $\mu_R(N, M) \leq 0$. If any of them is positive, the electron will escape to the leads. This constraint, plus the fact that N and M must be integers, creates hexagonal domains in the region where the

electrostatic potential forms a double-well shape along the nanotube. In these domains the charge configuration is stable [6]. Figures 11a, b and c show schematics of the charge stability diagram of a DQD in three different regimes, depending on the interdot coupling.

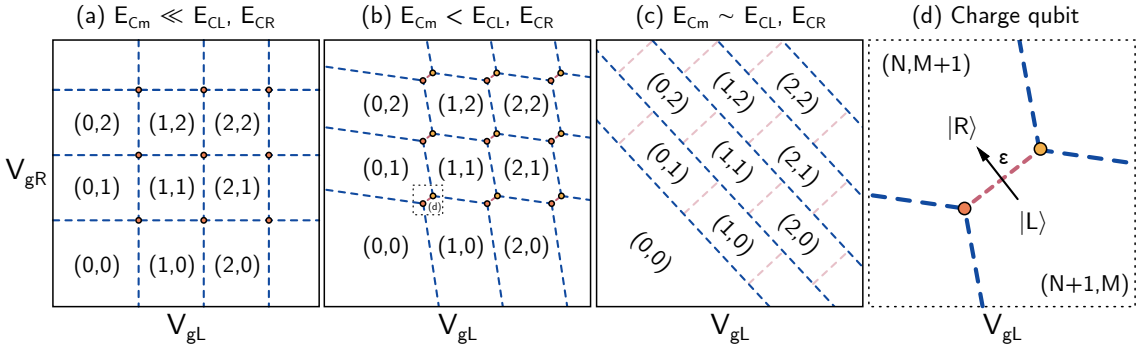

Figure 11: The geometry of the charge stability diagram of a double quantum dot depends on the mutual charging energy E_{Cm}. (a) Uncoupled QDs, (b) weakly coupled QDs, (c) strongly coupled DQDs. Dashed lines are charge transition lines. Circles indicate triple points. (d) The red dashed line represents the interdot charge transition. $|L\rangle$ and $|R\rangle$ indicate the presence of the electron in the left or right dot. ε is the energy detuning axis.

3.2.2 Charge qubits

The interdot charge transition (ICT) involves tunneling between the left and right quantum dots, as shown in Fig. 11d. The energy detuning (ε) quantifies the electrochemical potential difference between the two dots, while the tunneling energy (t_c) quantifies the tunneling rate between them [11]. The position of a single charge can be written as $|\psi\rangle = \alpha_L |L\rangle + \alpha_R |R\rangle e^{i\theta}$, using the charge basis $\{|L\rangle, |R\rangle\}$. The state $|L\rangle$ indicates the presence of the electron in the left dot, while $|R\rangle$ indicates the presence of the electron in the right dot. Using the same basis, the Hamiltonian of the DQD can be written as

$$\hat{H} = \frac{\varepsilon}{2}\hat{\sigma}_z + t_c\hat{\sigma}_x, \tag{16}$$

where $\hat{\sigma}_z$ and $\hat{\sigma}_x$ are the Pauli matrices. Diagonalizing Eq. (16) gives the energy eigenvalues,

$$E_\pm = \pm\frac{1}{2}\sqrt{\varepsilon^2 + 4t_c^2}. \tag{17}$$

The eigenstates $|\pm\rangle$ are used to build a qubit with transition frequency $\hbar\omega_q = E_+ - E_- = \sqrt{\varepsilon^2 + 4t_c^2}$.

The coherent tunneling between the two dots that characterizes the ICT implies that there is no current flowing through the DQD, from source to drain electrodes. Therefore, transport measurements cannot be used to read out the qubit state. Instead, we will couple another system to it, which is the superconducting resonator we describe in the next section.

4 Characterization of the superconducting cavity

Gate reflectometry readout is a technique that enables high frequency (MHz-GHz) and sensitive measurements of the impedance changes of a device under test [26]. This information is encoded in the reflected signal from a microwave resonator, also referred to as microwave cavity. With the goal of using this technique to measure the CNT QDs, our group has designed a new chip that integrates the trench where the nanotube is suspended and a superconducting cavity connected to one of the gate electrodes. This section describes the design and presents Sonnet simulation results for the cavity. We then introduce microwave resonator concepts and present the cavity's characterization.

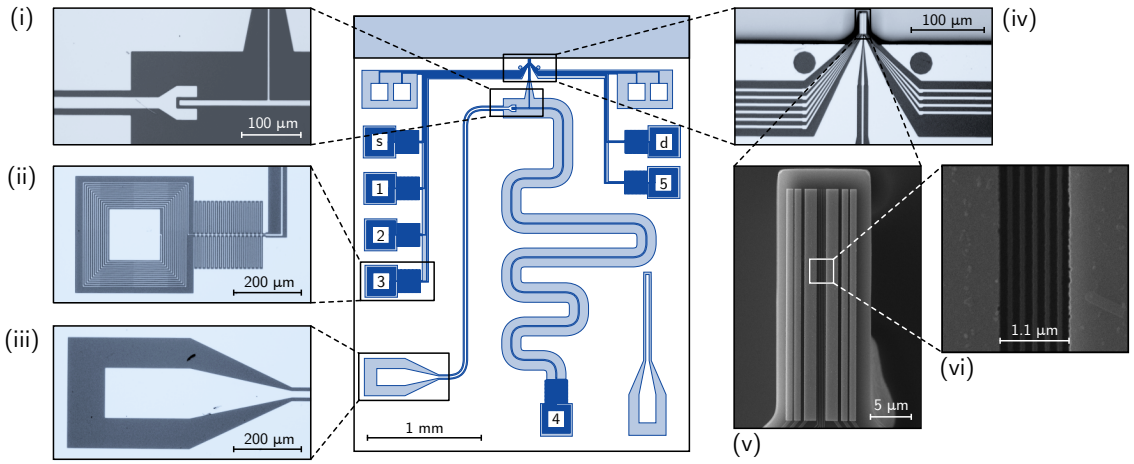

Figure 12: Integrated chip design. The enlarged views are micrographs of (i) coupling gap, (ii) LC filter, (iii) feedline, (iv), (v) and (vi) trench. The arabic numbers indicate the different pads: source (s), drain (d) and gates (1,2,3,4,5). The central meandering element is a $\lambda/4$ microwave resonator.

4.1 Integrated chip design

The layout of the integrated chip is shown in Fig. 12. The insets highlight the different parts of the chip: (i)-(iv) show optical microscope images; (v) and (vi), scanning electron microscope (SEM) micrographs. The central serpentine element of the chip is a $\lambda/4$ microwave resonator that serves both as a cavity for dispersive readout and an electrostatic gate (4) for the CNT. The numbered pads on the sides of the chip are the remaining electrodes: source (s), drain (d) and gates (1,2,3,5). Each electrode ends in a low-pass LC filter (ii). To send the radiofrequency (RF) signal to the cavity, we use the feedline (iii). The coupling between the cavity and the feedline can be controlled by their separation (i). Regarding the trench (iv), discussed in section 2, it is located on the top part of the chip. All the lines coming from the pads are connected to the trench. The insets (v) and (vi) show magnified views of it. The remaining RF line on the bottom right side of the chip serves as a driving line for the cavity. Chiral Nano's CNT transfer process uses the four small pads above the source and drain pads. Once the CNT has been placed on top of the trench, high voltages are applied to each pair of pads to cut the CNT, leaving it suspended. The transfer process is crucial, because of the incompatibility of CVD with superconducting materials.

4.1.1 Superconducting transition of niobium

A key aspect of the design is the use of a superconducting material for the cavity: in this case, niobium (Nb). One of the initial tests we have done is to ensure the niobium film is indeed superconducting, especially in the thinner part of the gate electrodes, where the area

of Nb is 100 nm ×100 nm. We measured a structure that mimics the gate electrodes using a four-point probe configuration, see Fig. 13a. It is more precise than the two-point probe configuration, as it avoids spurious resistances, like contact resistances. The two outer probes provide a steady current ($\sim$ nA), while the two inner probes measure the voltage drop across the path. We measured the resistance as a function of temperature, see Fig. 13b. The critical temperature we obtain is $T = 9.65\,\mathrm{K}$. The tabulated critical temperature of bulk Nb is 9.268 K, which indicates either a calibration shift of the thermometers in the cryostat or improper thermalization of the Nb sample.

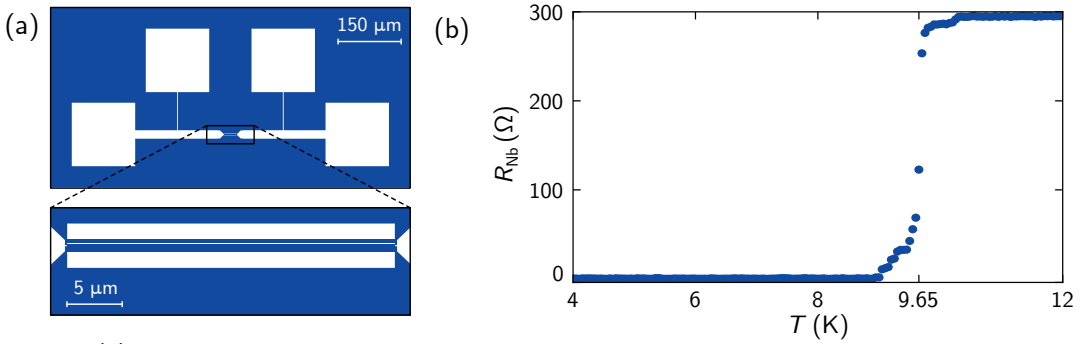

Figure 13: (a) 4 point probe structure of a 100 nm wide, 100 nm thick and 30 μm long Nb path. The environment reproduces the trench. (b) Measurement of superconducting transition of niobium.

4.1.2 Microwave cavity

The $\lambda/4$ microwave resonator is the central element of the chip. It is designed to create a standing wave pattern with maximum electric field at one of the nodes, in the region where the quantum dots will be defined. This ensures maximal coupling between the quantum dot's electric dipole and the electric field of the cavity. We operate the microwave cavity as a dispersive readout, in a regime where changes in the electric dipole associated with electronic transitions in the quantum dots renormalize the cavity frequency. The frequency shift reveals measurable information about the electronic transition in the quantum dots, and therefore, a readout mechanism. The meander geometry provides compactness while maintaining the quarter-wavelength electromagnetic path length necessary for the desired resonant frequency in the microwave range. For the design in Fig. 12, the length of the resonator is 6 mm, the calculated resonance frequency is $f_r = 6\,\mathrm{GHz}$, and the expected frequency shifts are on the order of 100 kHz to few MHz.

4.1.3 LC filters

The end of the $\lambda/4$ resonator that connects to the DC bias pad includes a distributed LC filter composed of interdigitated capacitor elements and an inductive coil to ensure proper electromagnetic boundary conditions and RF isolation [27]. The role of the low-pass LC filters is to avoid photonic losses from the cavity due to coupling of its electromagnetic field to the rest of the lines. These filters simultaneously act as an effective shunt to ground for photons at the resonance frequency. The ground reference established at the end of the cavity line creates the necessary voltage node for the $\lambda/4$ mode. This ensures that photons remain confined within the resonator structure, while being able to DC bias the cavity through that port for proper gate control.

4.2 Sonnet simulations

We have simulated the LC filters using Sonnet [28], to understand the effect of changing the number of turns of the inductor and the number of lines of the capacitor. This way,

we optimize the filter design and characterize its performance with respect to these parameters (Fig. 14). Sonnet is a specialized software for simulating planar circuits in the radiofrequency range. We input into the program the layer stack of the circuit: 500 µm of Si ($\varepsilon_r = 11.9$), 300 nm of SiO_2 ($\varepsilon_r = 3.9$), Nb configured as lossless metal[2] and 500 µm of air. Considering that the smallest features are 3 µm wide and the amount of computational resources needed for the simulation, the mesh size we use is 2 µm × 2 µm.

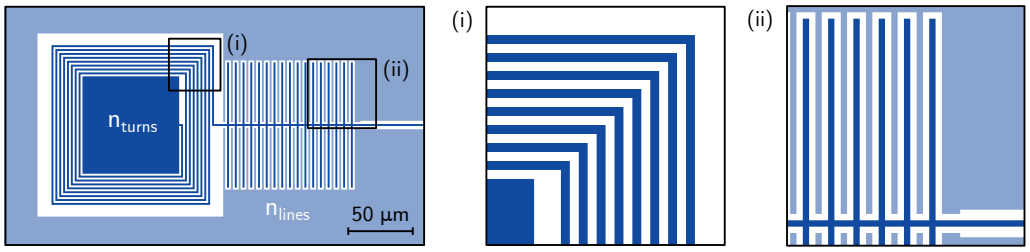

Figure 14: LC filter layout. The inductor has $n_{turns} = 8$ and the interdigitated capacitor has $n_{lines} = 17$. The tracks and the gaps are 3 µm wide. Insets (i) and (ii) are magnified views of the inductor and the capacitor, respectively. The external light blue region defines the ground plane.

We simulate a two-port, 50 Ω network: the input is connected to the pad inside the inductor and the output is connected to a pad at the end of the capacitor (not shown in Fig. 14). Sonnet outputs the scattering parameters of the circuit, which are complex numbers that describe how the circuit reflects and transmits signals at different frequencies. The reflection coefficient S_{11} is defined as the ratio of the reflected power to the incident power, while the transmission coefficient S_{21} is defined as the ratio of the transmitted power to the incident power. See Ref. [29] for a detailed explanation.

Simulations show that the number of turns of the inductor influences the transmission coefficient more than the number of capacitor lines. Figure 15a shows the value of the cutoff frequency[3] for different values of n_{turns} and n_{lines}. In Figure 15b we show the effect in the value of the transmission coefficient at 6 GHz, which is the designed resonance frequency of the circuit.

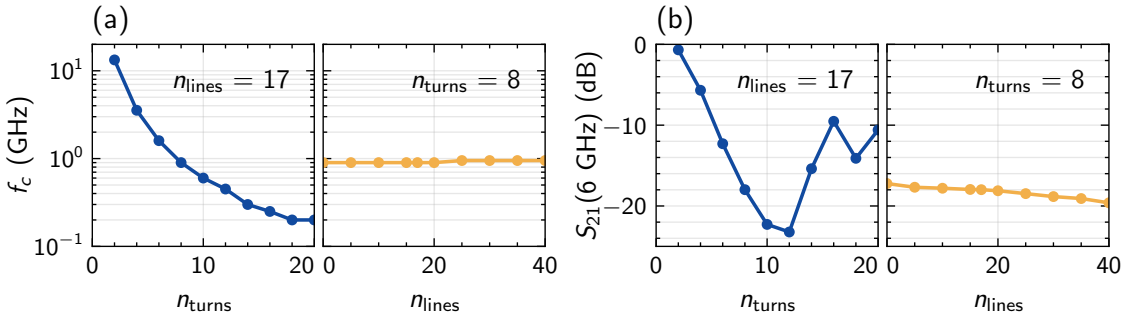

Figure 15: Sonnet simulation of the LC filter. The number of turns and the number of lines are varied to optimize (a) the cutoff frequency and (b) the attenuation at the resonance frequency. See Appendix C for more details.

The values in the fabricated chips are $n_{\text{turns}} = 8$ and $n_{\text{lines}} = 17$, a good compromise between compactness and performance. The output of the corresponding Sonnet simulation is shown in Fig. 16. Next to it, we show the experimental transmission measurement for a

[2]A lossless metal in Sonnet is treated as a perfect electric conductor, with infinite conductivity and zero penetration length. For this reason, Sonnet does not need a thickness value.

[3]The cutoff frequency is defined as the frequency at which the transmission coefficient S_{21} drops −3 dB.

single distributed LC filter as in Fig. 14, in a helium dewar at 4 K. There is good agreement between the simulation and the measurements, both in the trend of the transmission and in the value of the cutoff frequency. Extra RF components in the dewar, as well as chip imperfections and the presence of wirebonds, add frequency-dependent losses that can be seen as wiggles and dips in the transmission of Fig. 16.

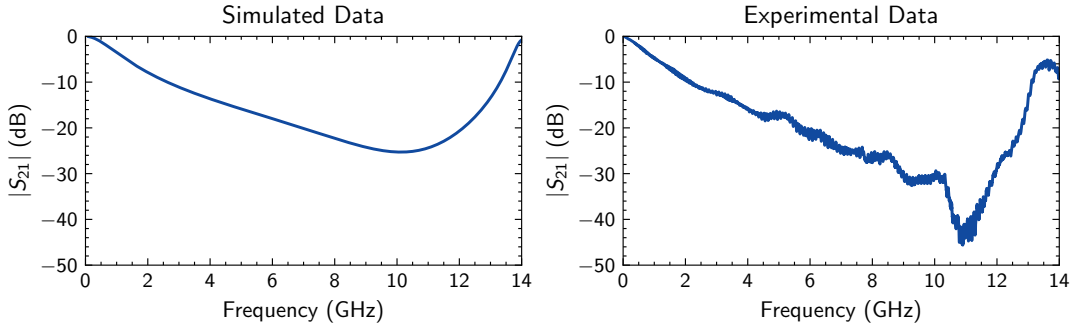

Figure 16: Sonnet simulation of the LC filter compared to experimental measurements.

To finish this section, we have to mention that Sonnet simulations of the device shown in Fig. 12, which include the cavity, also agree with experimental measurements performed both at 4 K and at mK temperatures. See Fig. 30 in Appendix C.

4.3 Resonator characterization

In this section we first introduce some basic concepts of resonators, to then present the results of the characterization of the cavity.

4.3.1 Basics of reflectometry

All resonators can be described in terms of three parameters: the resonance frequency f_r, the total or loaded quality factor Q_l and the coupling coefficient β [30]. The quality factor Q_l is defined as the ratio of the average energy stored in the resonator to the energy lost per cycle. It can be written as $Q_l = \omega_r/\kappa$, where $\omega_r = 2\pi f_r$ is the angular resonance frequency and κ is the total decay rate of the resonator. The decay rate κ can be written as the sum of the *external* and *internal* damping rates $\kappa = \kappa_{\text{ext}} + \kappa_{\text{int}}$. The external losses are via the coupling to the external circuit, which is used for measurement, while the internal losses are uncontrolled losses to the environment. The corresponding quality factors can be defined as $Q_{\text{ext}} = \omega_r/\kappa_{\text{ext}}$ and $Q_{\text{int}} = \omega_r/\kappa_{\text{int}}$, with $Q_l^{-1} = Q_{\text{ext}}^{-1} + Q_{\text{int}}^{-1}$. The ratio of the internal quality factor to the external quality factor defines the coupling coefficient

$$\beta = \frac{Q_{\text{int}}}{Q_{\text{ext}}}. \tag{18}$$

This coefficient describes the coupling strength between the resonator and the external circuit. Three regimes of coupling can be distinguished: undercoupled ($\beta < 1$), critically coupled ($\beta = 1$) and overcoupled ($\beta > 1$). See the examples in Fig. 17. Critical coupling occurs when the internal and external losses are equal, and the impedance is matched between the resonator and the input line.

The reflectometry measurements involve measuring the reflected signal. The reflection coefficient S_{11} of a resonator can be written in terms of external and internal quality factors and the resonance frequency as follows [30]

$$S_{11} = \frac{Q_{\text{ext}} - Q_{\text{int}} + 2iQ_{\text{int}}Q_{\text{ext}}\frac{\omega-\omega_r}{\omega_r}}{Q_{\text{ext}} + Q_{\text{int}} + 2iQ_{\text{int}}Q_{\text{ext}}\frac{\omega-\omega_r}{\omega_r}}. \tag{19}$$

Note that when $\omega = \omega_r$, $\arg(S_{11}) = 0$ and $|S_{11}| = |1-\beta|/(1+\beta)$. When the resonator is critically coupled ($\beta = 1$) the reflection coefficient is minimized: $|S_{11}| = 0$. It is in this limit that the reflected signal is most sensitive to changes in the resonator, and therefore the regime we want to operate in.

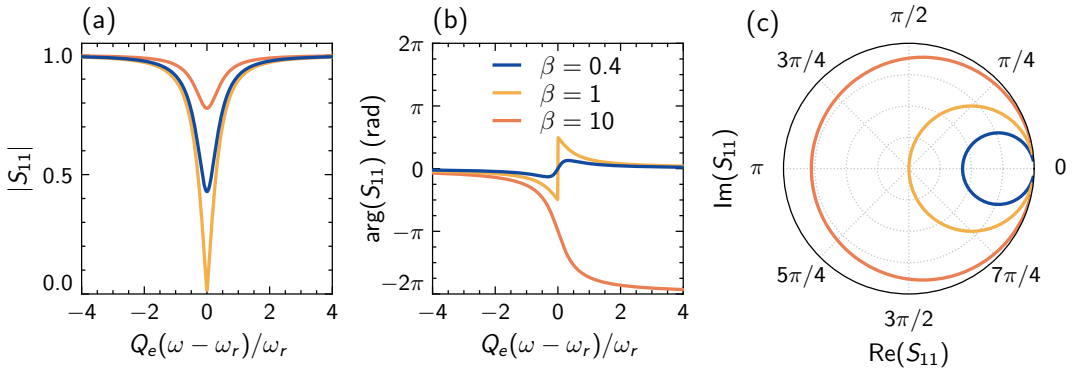

Figure 17: Three regimes of coupling: undercoupled ($\beta < 1$), critically coupled ($\beta = 1$) and overcoupled ($\beta > 1$). The reflection coefficient S_{11} is plotted as a function of frequency. (a) Magnitude, (b) phase, (c) complex plane. The diameter of the complex plane circle is $d = 2\beta/(1+\beta)$. Adapted from Ref. [30].

4.3.2 Data fitting procedure

To study the superconducting cavity at cryogenic temperatures, we use a Proteox™ dilution refrigerator from Oxford Instruments. The setup is equipped with a vector network analyzer (VNA) that we use to measure the reflection coefficient S_{11} of the cavity when connected to the driving line. The VNA outputs the complex reflection coefficient S_{11} as a function of frequency, up to 14 GHz.

The standard procedure to extract the parameters f_r, Q_e and Q_i is to fit the data to Eq. (19). One of the tasks of this thesis has been to improve the fitting process to make it more robust and user-friendly. We have written a script that uses the NLQFIT-7 algorithm [31, 32], which allows us to fit complex data directly, as opposed to older procedures used in the group that fitted magnitude and phase separately [33].

A graphical user interface has been developed to facilitate the navigation through data files and selection of fitting regions. Then, the script applies a baseline correction to the data and fits a more convoluted version of Eq. (19), which includes correction terms to account for various non-idealities in the measurement setup. See Eq. (33) in Appendix D. This makes the fitting process more robust and the resulting quality factors more accurate. We stress here the importance of precise fitting of the cavity response, since it is this response that will give us information about the system. More information about the algorithm and the code used can be found in Appendix D.

We have measured the resonance of a cavity integrated on a chip as in Fig. 12 at different temperatures, from 6 K to 25 mK. The behavior of the extracted parameters is shown in Fig. 18. The resonance frequency is constant ($f_r = 5.884$ GHz) below 2 K and it decreases at higher temperatures. The quality factors behave similarly ($Q_i = 1150$ and $Q_e = 1730$), but Q_i shows a jump at $T = 1.14$ K, which corresponds to the superconducting transition of the aluminum used to wirebond the chip to the sample holder [11].

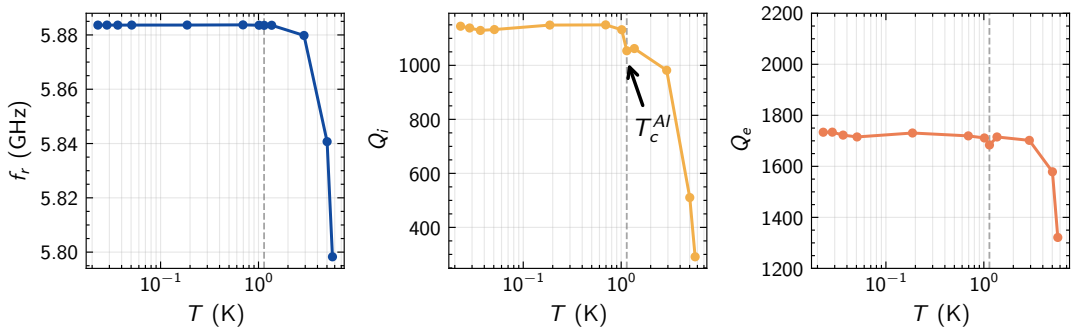

Figure 18: The values of the resonance frequency f_r, internal quality factor Q_i and external quality factor Q_e decrease as the temperature increases. The data is fitted to Eq. (19). The dashed vertical line indicates the superconducting transition of aluminum at 1.14 K. At low temperatures, $\beta = 0.66$, which indicates that the cavity is undercoupled.

5 Readout of charge states in the integrated device

5.1 Reflectometry readout

We have already mentioned that the reflectometry readout technique detects changes in the impedance of the device under test by measuring the reflected signal from a microwave resonator. In the context where DQDs are defined, the charge transitions can be modelled as an effective capacitance change ΔC [26]. The resonator couples capacitively to the quantum dot through the gate, and changes in the resonator capacitance generate changes in the magnitude and phase of the reflected signal.

Let us consider a simple example to gain some intuition. Following Ref. [34], we model the resonator as a series RLC circuit with impedance

$$Z(\omega) = i\omega L + \frac{1}{i\omega C} + R. \tag{20}$$

The resonance happens when the frequency fulfills $\arg(Z) = 0$. Imposing this condition to Eq. (20), the expression for the resonance frequency is given by

$$f_r = \frac{1}{2\pi\sqrt{LC}}. \tag{21}$$

We see that the resonance frequency is sensitive to changes in the capacitance C, as those provoked by electronic transitions. If we drive the cavity at a fixed frequency f_r and measure the reflected signal S_{11}, we can detect changes in the capacitance by observing shifts in the resonance frequency.

Figure 19 shows an example of a measurement. We quantify resonance shifts via changes in the magnitude $|S_{11}|$ and phase $\arg(S_{11})$ of the reflected signal (Fig. 19a, 19b). The shift in the complex plane combines both components (Fig. 19c):

$$|\Delta S_{11}| = \sqrt{[\mathrm{Re}(\Delta S_{11})]^2 + [\mathrm{Im}(\Delta S_{11})]^2}. \tag{22}$$

The greater the shift, the bigger the signal to noise ratio (SNR) will be.

5.2 Experimental results

We now show some of the measurements from the first functional integrated chips we have produced. The following measurements, as well as the modulation curves in Fig. 5 from Section 2.4, correspond to the same device.

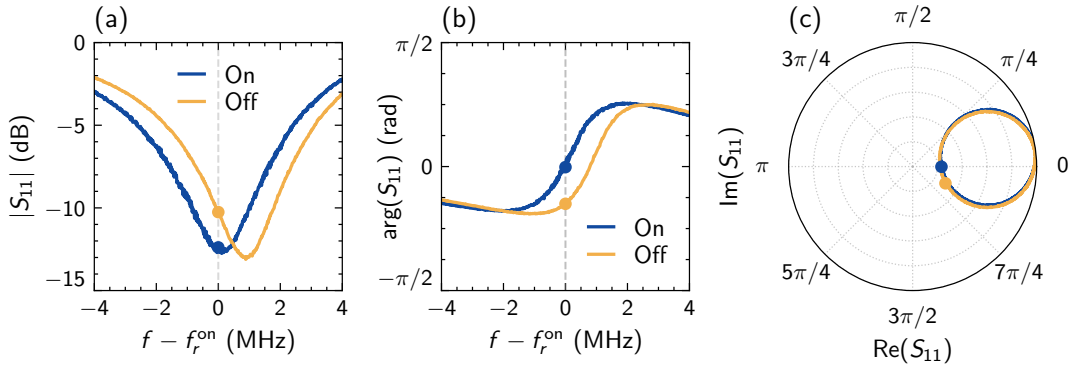

Figure 19: The resonance is shifted when the coupling of the cavity to the quantum dots changes. On the "on" state, the cavity is coupled to an electronic transition between two quantum dots, and on the "off" state, it is not. We quantify the shift via the distance $|\Delta S_{11}|$ in the complex plane. The data has been extracted from the interdot charge transition in Fig. 26.

5.2.1 Conductance measurement

The data in Fig. 8 is a zoom of the conductance measurement shown in Fig. 20. The data from a simultaneous reflectometry measurement is also shown in the bottom panel of Fig. 20, demonstrating the success of this readout technique.

On the left, we see the Fabry-Pérot region, where holes behave as coherent wave packets that undergo quantum interference [35]. The conductance remains high throughout this region. The band gap is the 150 mV region after the peak at 1 V, where the conductance drops to zero. Using the lever arm $\alpha_g \sim 0.2\,\mathrm{eV/V}$ calculated in Section 3.1.3, the energy gap between the conduction and valence bands is $E_{\mathrm{gap}} \sim 30\,\mathrm{meV}$. The right side of the figure shows the Coulomb blockade peaks for single electrons, featuring the characteristic four-fold degeneracy of CNTs.

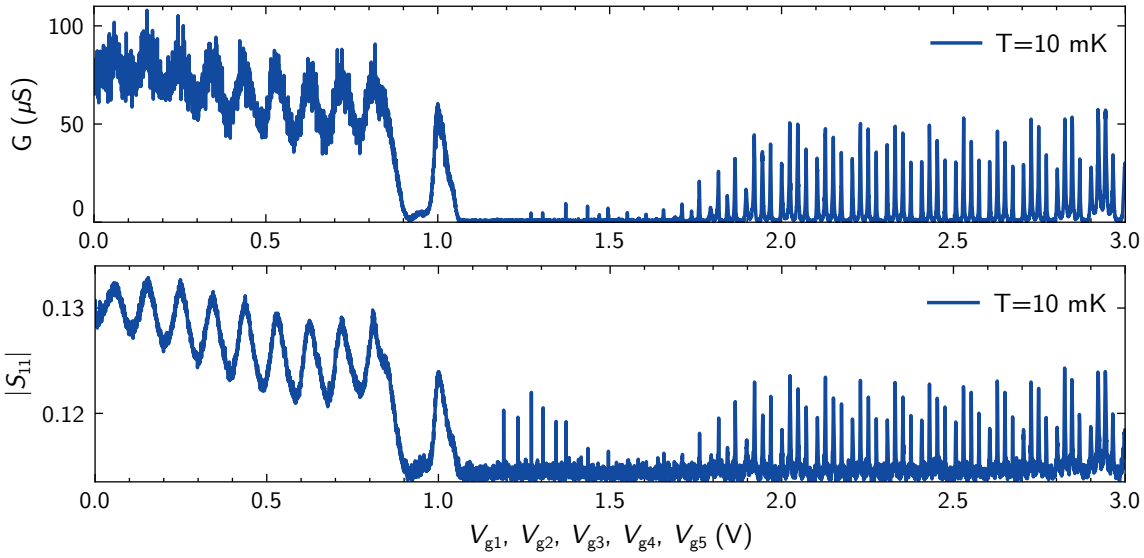

Figure 20: (Top) Measurement of the conductance as a function of the gate voltages. (Bottom) Simultaneous reflectometry measurement. The Fabry-Pérot region is visible in the hole region (left), as well as the Coulomb blockade peaks for single electrons (right). Fig. 8 is a zoom of the top figure.

5.2.2 Coulomb diamonds

Figures 21 and 22 show the Coulomb diamonds measured using transport and reflectometry, respectively. In this case, only the third gate has been swept, while the remaining gates are held at 0 V. The largest diamond at $V_{g3} = -0.4$ V marks th band gap. We see that diamonds appear on the left side, for negative gate voltages, indicating we are confining holes instead of electrons, as in Fig. 20. A possible explanation is that adsorbed molecules or contamination can alter nanotube doping, changing the carrier type that shows low conductance. Moreover, the diamonds are not regular, their size becomes smaller as they get further from the gap.

These electronic transitions involve incoherent tunneling, which appears primarily as changes in resistance of the load. Therefore, the signal is visible in the magnitude of the reflection coefficient $|S_{11}|$. When the transitions are coherent, like in the case of the interdot charge transition we will present later, the electron is isolated between the two dots and there are no dissipative losses. In that case, the phase of the reflected signal is more sensitive to the changes than magnitude.

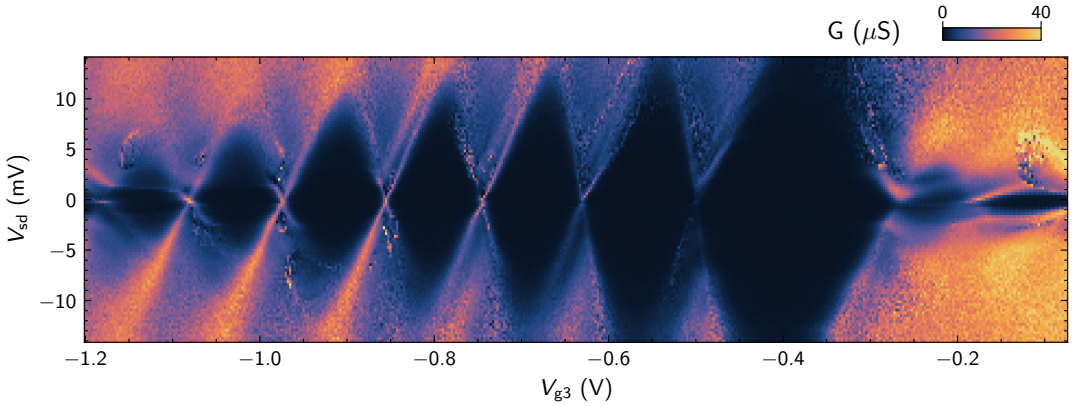

Figure 21: Coulomb diamonds measured in transport. We vary the voltage of the third gate, while the remaining gates are held at 0 V. The largest diamond corresponds to the gap between conduction and valence band.

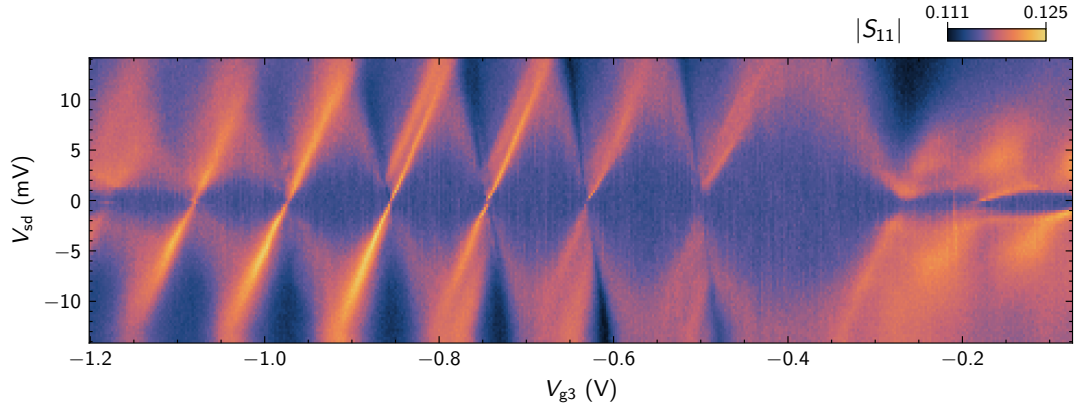

Figure 22: Coulomb diamonds measured using reflectometry. The cavity couples to the quantum dots successfully, allowing to observe diamonds as changes in the magnitude of the reflected signal.

5.2.3 Charge stability diagrams

Fig. 23 shows the measured charge stability diagram. Single and double dot regions are visible, which have the appearance described in Fig. 11b and c. Figure 24 shows a closer view of the honeycomb pattern in the DQD region.

Zooming even more, we can see the interdot charge transition, in which the electrochemical potentials of the two dots align, but are far from the potentials of the electrodes (Figs. 25 and 26). The ICT measurement clearly shows the advantage of reflectometry. This feature is not visible in transport measurements, where only two finite conductance regions appear: the triple points. This is because there is no net charge flowing to the leads, the electron tunnels coherently between the two dots. The reflected signal S_{11} shows a clear change in the phase and magnitude. This transition can be used to define a charge qubit in future experiments (Sec. 3.2.2).

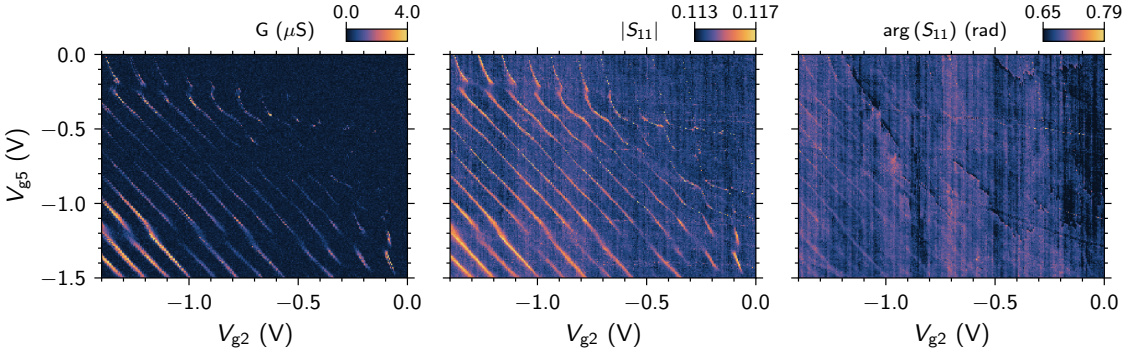

Figure 23: Charge stability diagram measured using reflectometry. Single dot features are visible in the bottom left corner, where straight diagonal lines appear. The top right region shows a faint honeycomb region. See Fig. 24 for a zoom of this area.

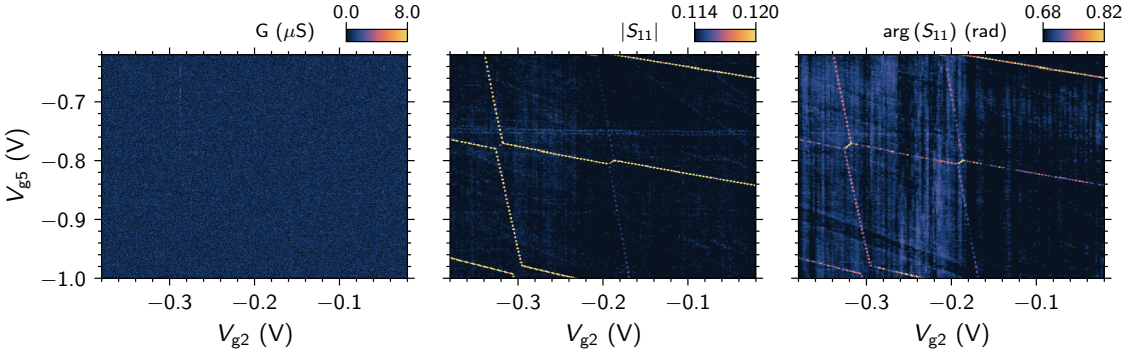

Figure 24: Honeycomb pattern, indicating the presence of a double quantum dot. The charge transition lines are visible only in the reflectometry readout, not in transport, where conductance G remains at zero.

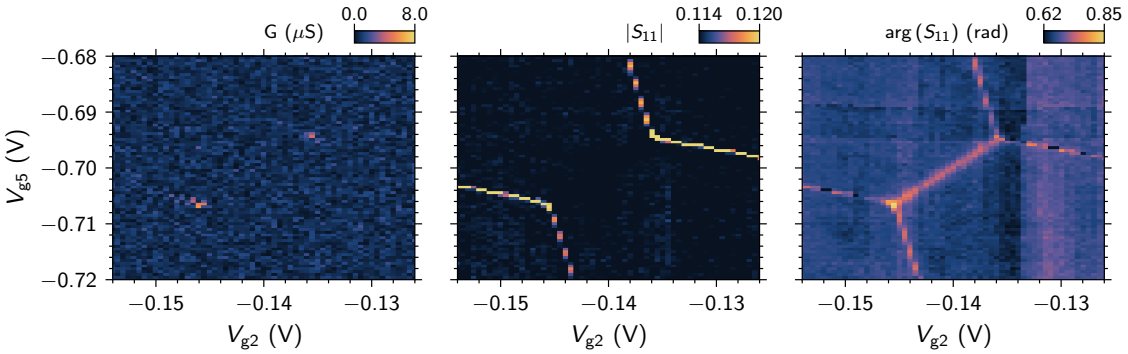

Figure 25: Example of an ICT measurement. In transmission, only two finite conductance regions appear at the triple points. In reflectometry, a clear change in the phase and magnitude is visible. In this example, the frequency shift is small in the ICT region, so the magnitude does not change appreciably. It is enough, however, to produce a clear change in the phase.

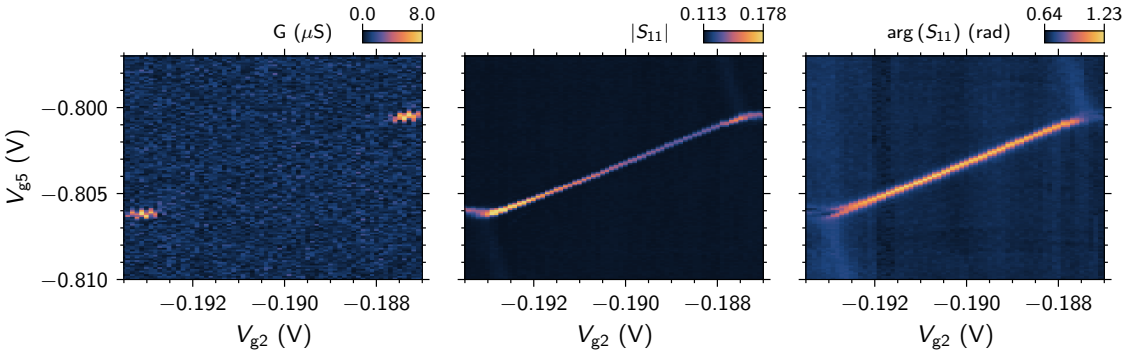

Figure 26: The same transition as in Fig. 25 after the height of the interdot barrier has been modified to enhance the detected signal. In this example the ICT is measurable both in magnitude and phase. Transport only shows the bias points. The data to illustrate the frequency shift in Fig. 19 has been taken "on" and "off" the transition.

6 Conclusion

The integrated platform we have developed opens numerous possibilities for quantum opto-electromechanical experiments, perfectly aligning with the research focus of our group at ICFO.

Defining high-quality charge qubits enables us to study qubit coupling to different degrees of freedom. This includes fermionic degrees of freedom, such as electron spin, which forms the basis for spin qubits [36], a highly relevant field in quantum technologies. It also covers bosonic degrees of freedom, including photons [7] and phonons [5], which would allow investigating how qubits interact with mechanical vibrations of the suspended nanotube in our platform. Achieving sufficiently coherent qubits is a prerequisite for all experiments in these directions.

Regarding the device studied, we have demonstrated dispersive readout of interdot charge transitions in a suspended carbon nanotube quantum dot coupled to a superconducting microwave cavity. The device resonates at $f_r = 5.88\,\mathrm{GHz}$ with internal and external quality factors $Q_i = 1150$ and $Q_e = 1730$. We observe clear Coulomb diamonds and honeycomb stability diagrams through shifts in the reflectometry signal at interdot charge transitions, absent in DC transport. Upcoming experiments will drive the qubit through a gate with an external radiofrequency tone, enabling qubit spectroscopy and a systematic study of how the interdot barrier tunes the qubit energy splitting. Experiments that tune the cavity into resonance with the qubit, allowing coherent energy exchange between the two systems, are also in preparation.

The nanotube stamping process will be optimized in the near future. A new generation of stapled nanotubes will allow statistical studies and improved control over their mechanical resonance frequency.

Regarding microwave cavity improvements, the new devices will feature narrower gate widths and a shorter trench, raising the natural mechanical frequency. The group is also developing new on-chip filters and exploring NbN as the superconducting material; its high kinetic inductance offers magnetic-field resilience and enables greater miniaturization and compactness. Finally, increasing the device density per wafer will boost the fabrication yield.

References

[1] S. Iijima, "Helical microtubules of graphitic carbon", Nature **354**, 56–58 (1991) DOI: 10.1038/354056a0 (cit. on pp. 1, 2).

[2] A. Jorio, G. Dresselhaus, and M. S. Dresselhaus, eds., *Carbon Nanotubes: Advanced Topics in the Synthesis, Structure, Properties and Applications*, Vol. 111, Topics in Applied Physics (Springer Berlin Heidelberg, Berlin, Heidelberg, 2008), DOI: 10.1007/978-3-540-72865-8 (cit. on p. 1).

[3] E. A. Laird, F. Kuemmeth, G. A. Steele, K. Grove-Rasmussen, J. Nygård, K. Flensberg, and L. P. Kouwenhoven, "Quantum transport in carbon nanotubes", Reviews of Modern Physics **87**, 703–764 (2015) DOI: 10.1103/RevModPhys.87.703 (cit. on pp. 1, 2, 5, 7).

[4] R. Hanson, L. P. Kouwenhoven, J. R. Petta, S. Tarucha, and L. M. K. Vandersypen, "Spins in few-electron quantum dots", Reviews of Modern Physics **79**, 1217–1265 (2007) DOI: 10.1103/RevModPhys.79.1217 (cit. on pp. 1, 5, 8).

[5] C. Samanta, S. L. De Bonis, C. B. Møller, R. Tormo-Queralt, W. Yang, C. Urgell, B. Stamenic, B. Thibeault, Y. Jin, D. A. Czaplewski, F. Pistolesi, and A. Bachtold, "Nonlinear nanomechanical resonators approaching the quantum ground state", Nature Physics **19**, 1340–1344 (2023) DOI: 10.1038/s41567-023-02065-9 (cit. on pp. 1, 20).

[6] W. G. Van Der Wiel, S. De Franceschi, J. M. Elzerman, T. Fujisawa, S. Tarucha, and L. P. Kouwenhoven, "Electron transport through double quantum dots", Reviews of Modern Physics **75**, 1–22 (2002) DOI: 10.1103/RevModPhys.75.1 (cit. on pp. 1, 9, 10, 24).

[7] A. Blais, A. L. Grimsmo, S. M. Girvin, and A. Wallraff, "Circuit quantum electrodynamics", Reviews of Modern Physics **93**, 025005 (2021) DOI: 10.1103/RevModPhys.93.025005 (cit. on pp. 1, 20).

[8] Y. Chu, P. Kharel, T. Yoon, L. Frunzio, P. T. Rakich, and R. J. Schoelkopf, "Creation and control of multi-phonon Fock states in a bulk acoustic-wave resonator", Nature **563**, 666–670 (2018) DOI: 10.1038/s41586-018-0717-7 (cit. on p. 1).

[9] M. Muoth and C. Hierold, "Transfer of carbon nanotubes onto microactuators for hysteresis-free transistors at low thermal budget", in 2012 IEEE 25th International Conference on Micro Electro Mechanical Systems (MEMS) (Jan. 2012), pp. 1352–1355, DOI: 10.1109/MEMSYS.2012.6170417 (cit. on pp. 1, 3).

[10] T. Althuon, T. Cubaynes, A. Auer, C. Sürgers, and W. Wernsdorfer, "Nano-assembled open quantum dot nanotube devices", Communications Materials **5**, 5 (2024) DOI: 10.1038/s43246-023-00439-3 (cit. on pp. 1, 3).

[11] R. Tormo Queralt, "A non-linear carbon nanotube mechanical resonator near the quantum ground state of motion" (Universitat Politècnica de Catalunya, Nov. 18, 2024), DOI: 10.5821/dissertation-2117-427534 (cit. on pp. 1–3, 6, 7, 10, 15).

[12] L. E. F. Foa Torres, S. Roche, and J.-C. Charlier, *Introduction to Graphene-Based Nanomaterials: From Electronic Structure to Quantum Transport*, 2nd ed. (Cambridge University Press, Jan. 30, 2020), DOI: 10.1017/9781108664462 (cit. on pp. 1, 3).

[13] K. S. Novoselov, A. K. Geim, S. V. Morozov, D. Jiang, Y. Zhang, S. V. Dubonos, I. V. Grigorieva, and A. A. Firsov, "Electric Field Effect in Atomically Thin Carbon Films", Science **306**, 666–669 (2004) DOI: 10.1126/science.1102896 (cit. on p. 2).

[14] S. M.-M. Dubois, Z. Zanolli, X. Declerck, and J.-C. Charlier, "Electronic properties and quantum transport in Graphene-based nanostructures", The European Physical Journal B **72**, 1–24 (2009) DOI: 10.1140/epjb/e2009-00327-8 (cit. on p. 2).

[15] S. Ilani and P. L. McEuen, "Electron Transport in Carbon Nanotubes", Annual Review of Condensed Matter Physics **1**, 1–25 (2010) DOI: 10.1146/annurev-conmatphys-070909-103928 (cit. on p. 2).

[16] *Argonne National Laboratory Homepage*, Argonne National Laboratory, `https://www.anl.gov/` (visited on 08/19/2025) (cit. on p. 3).

[17] *Chiral Nano Homepage*, Chiral Nano AG, (2025) `https://www.chiralnano.com/` (visited on 08/19/2025) (cit. on p. 3).

[18] J. Waissman, M. Honig, S. Pecker, A. Benyamini, A. Hamo, and S. Ilani, "Realization of pristine and locally tunable one-dimensional electron systems in carbon nanotubes", Nature Nanotechnology **8**, 569–574 (2013) DOI: 10.1038/nnano.2013.143 (cit. on p. 3).

[19] G. D. Nessim, "Properties, synthesis, and growth mechanisms of carbon nanotubes with special focus on thermal chemical vapor deposition", Nanoscale **2**, 1306 (2010) DOI: 10.1039/b9nr00427k (cit. on p. 3).

[20] K. A. Shah and B. A. Tali, "Synthesis of carbon nanotubes by catalytic chemical vapour deposition: A review on carbon sources, catalysts and substrates", Materials Science in Semiconductor Processing **41**, 67–82 (2016) DOI: 10.1016/j.mssp.2015.08.013 (cit. on pp. 3, 6).

[21] L. P. Kouwenhoven, C. M. Marcus, P. L. McEuen, S. Tarucha, R. M. Westervelt, and N. S. Wingreen, "Electron Transport in Quantum Dots", in *Mesoscopic Electron Transport*, edited by L. L. Sohn, L. P. Kouwenhoven, and G. Schön (Springer Netherlands, Dordrecht, 1997), pp. 105–214, DOI: 10.1007/978-94-015-8839-3_4 (cit. on p. 5).

[22] T. Ihn, *Semiconductor nanostructures: quantum states and electronic transport* (Oxford University Press, New York, NY, 2010), 568 pp. (cit. on pp. 5, 6).

[23] L. P. Kouwenhoven, D. G. Austing, and S. Tarucha, "Few-electron quantum dots", Reports on Progress in Physics **64**, 701 (2001) DOI: 10.1088/0034-4885/64/6/201 (cit. on p. 6).

[24] C. W. J. Beenakker, "Theory of Coulomb-blockade oscillations in the conductance of a quantum dot", Physical Review B **44**, 1646–1656 (1991) DOI: 10.1103/PhysRevB.44.1646 (cit. on p. 6).

[25] R. Leturcq, C. Stampfer, K. Inderbitzin, L. Durrer, C. Hierold, E. Mariani, M. G. Schultz, F. Von Oppen, and K. Ensslin, "Franck–Condon blockade in suspended carbon nanotube quantum dots", Nature Physics **5**, 327–331 (2009) DOI: 10.1038/nphys1234 (cit. on p. 8).

[26] P. Apostolidis, B. J. Villis, J. F. Chittock-Wood, J. M. Powell, A. Baumgartner, V. Vesterinen, S. Simbierowicz, J. Hassel, and M. R. Buitelaar, "Quantum paraelectric varactors for radiofrequency measurements at millikelvin temperatures", Nature Electronics **7**, 760–767 (2024) DOI: 10.1038/s41928-024-01214-z (cit. on pp. 11, 16).

[27] F.-E. Von Horstig, D. J. Ibberson, G. A. Oakes, L. Cochrane, D. F. Wise, N. Stelmashenko, S. Barraud, J. A. Robinson, F. Martins, and M. F. Gonzalez-Zalba, "Multimodule microwave assembly for fast readout and charge-noise characterization of silicon quantum dots", Physical Review Applied **21**, 044016 (2024) DOI: 10.1103/PhysRevApplied.21.044016 (cit. on p. 12).

[28] *Sonnet*, version 18.58, Sonnet Software LLC, 2024 (cit. on p. 12).

[29] D. M. Pozar, *Microwave engineering*, 4th ed (Wiley, Hoboken, NJ, 2012), 732 pp. (cit. on p. 13).

[30] D. J. Ibberson, "Dispersive readout of industrially-fabricated silicon quantum dots" (University of Bristol, Bristol, 2021) (cit. on pp. 14, 15).

[31] A. P. Gregory, P. D. Woolliams, and S. M. Hanham, "Robust Algorithms for Fitting Q-Factor in the Complex Domain", IEEE Access **12**, 188336–188348 (2024) DOI: 10.1109/ACCESS.2024.3514707 (cit. on pp. 15, 28).

[32] A. P. Gregory, *Q-factor measurement by using a Vector Network Analyser* (National Physical Laboratory, Jan. 4, 2022), DOI: 10.47120/npl.MAT58 (cit. on pp. 15, 28).

[33] J. Gao, "The Physics of Superconducting Microwave Resonators" (California Institute of Technology Pasadena, California, 2018) (cit. on p. 15).

[34] F. Vigneau, F. Fedele, A. Chatterjee, D. Reilly, F. Kuemmeth, M. F. Gonzalez-Zalba, E. Laird, and N. Ares, "Probing quantum devices with radio-frequency reflectometry", Applied Physics Reviews **10**, 021305 (2023) DOI: 10.1063/5.0088229 (cit. on p. 16).

[35] W. Yang, C. Urgell, S. L. De Bonis, M. Margańska, M. Grifoni, and A. Bachtold, "Fabry-Pérot Oscillations in Correlated Carbon Nanotubes", Physical Review Letters **125**, 187701 (2020) DOI: 10.1103/PhysRevLett.125.187701 (cit. on p. 17).

[36] L. M. K. Vandersypen, H. Bluhm, J. S. Clarke, A. S. Dzurak, R. Ishihara, A. Morello, D. J. Reilly, L. R. Schreiber, and M. Veldhorst, "Interfacing spin qubits in quantum dots and donors—hot, dense, and coherent", npj Quantum Information **3**, 34 (2017) DOI: 10.1038/s41534-017-0038-y (cit. on p. 20).

A Complementary Coulomb diamonds

This appendix contains the Coulomb diamond measurement that corresponds to the peaks shown in Fig. 8. This data is not shown in the main text because the diamonds are not as clear as the ones in Fig. 22, but they still allow to extract the parameters of the constant interaction model.

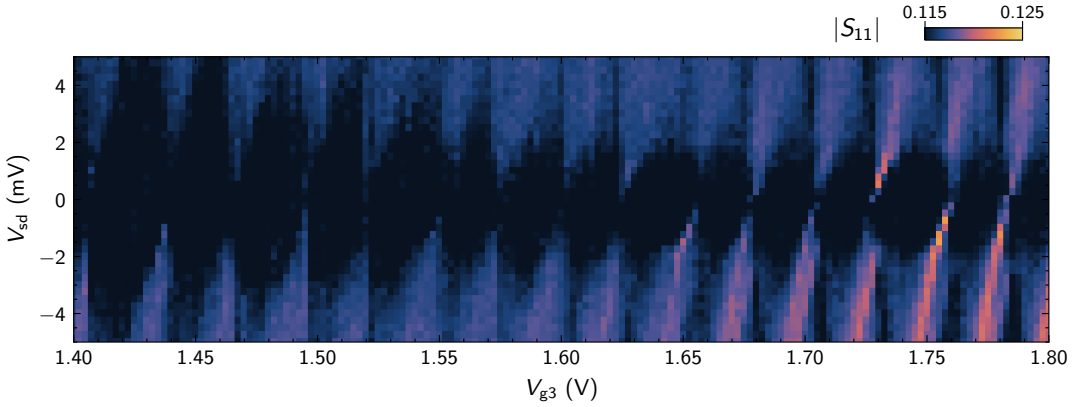

Figure 27: Coulomb diamonds measured using reflectometry.

From this measurement, we extract the following parameters:

$$E_C/\alpha_g = 24 \pm 1\,\mathrm{mV}, \qquad E_C = 4.9 \pm 0.5\,\mathrm{mV},$$
$$E_{add}/\alpha_g = 32.3 \pm 0.6\,\mathrm{mV}, \qquad E_{add} = 7.5 \pm 0.9\,\mathrm{mV}.$$

Which yield a lever arm $\alpha_g = 0.21 \pm 0.02$ eV/V. To complete the set of parameters given in the text, we also calculate the effective dot length L, the total capacitance C and the gate capacitance C_g:

$$L = 900 \pm 100\,\mathrm{nm},$$
$$C = 33 \pm 3\,\mathrm{aF},$$
$$C_g = 7 \pm 1\,\mathrm{aF}.$$

B Supplementary equations for double quantum dots

This appendix contains additional equations of quantum dot transport theory, which are not included in the main text. We followed the derivation from Ref. [6].

For the sake of completeness, we restate the equation for the total energy of a single quantum dot, Eq. (9),

$$U(N) = \frac{\left[-e\left(N - N_0\right) + C_\mathrm{g}V_\mathrm{g} + C_\mathrm{s}V_\mathrm{s} + C_\mathrm{d}V_\mathrm{d}\right]^2}{2C} + \sum_{n=1}^{N} E_n. \tag{23}$$

The total energy of the double quantum dot system, ignoring the single-particle energy levels is given by

$$\begin{aligned} U\left(N,M\right) =& \frac{1}{2}N^2E_{CL} + \frac{1}{2}M^2E_{CR} + NME_{Cm} \\ &- \frac{1}{e}\left[C_\mathrm{gL}V_\mathrm{gL}\left(NE_{CL} + ME_{Cm}\right) + C_\mathrm{gR}V_\mathrm{gR}\left(NE_{Cm} + ME_{CR}\right)\right] \\ &+ \frac{1}{e^2}\left[\frac{1}{2}C_\mathrm{gL}^2V_\mathrm{gL}^2E_{CL} + \frac{1}{2}C_\mathrm{gR}^2V_\mathrm{gR}^2E_{CR} + C_\mathrm{gL}V_\mathrm{gL}C_\mathrm{gR}V_\mathrm{gR}E_{Cm}\right]. \end{aligned} \tag{24}$$

where E_{CL} and E_{CR} are the charging energies of the individual dots, E_{Cm} is the electrostatic coupling energy, and $e > 0$ is the absolute value of the charge of the electron. The coupling energy E_{Cm} quantifies the change in the energy of one dot when an electron is added to the other dot. The expressions of the charging energies are

$$E_{CL} = \frac{e^2}{C_\mathrm{L}} \left(\frac{1}{1 - \frac{C_\mathrm{m}^2}{C_\mathrm{L} C_\mathrm{R}}} \right), \quad E_{CR} = \frac{e^2}{C_\mathrm{R}} \left(\frac{1}{1 - \frac{C_\mathrm{m}^2}{C_\mathrm{L} C_\mathrm{R}}} \right), \quad E_{Cm} = \frac{e^2}{C_\mathrm{m}} \left(\frac{1}{\frac{C_\mathrm{L} C_\mathrm{R}}{C_\mathrm{m}^2} - 1} \right). \tag{25}$$

with $C_{\mathrm{L(R)}} = C_{\mathrm{s(d)}} + C_{\mathrm{gL(R)}} + C_\mathrm{m}$, the sum of capacitances connected to the left (right) dot. E_{CL} and E_{CR} can be seen as the charging energies of the single dots multiplied by a correction factor, which vanishes when $C_\mathrm{m} = 0$.

A sanity check for the expressions (14) and (15) of the electrochemical potentials of the two dots is to verify that they yield the charging energies when adding electrons to the dots:

$$\mu_L(N+1, M) - \mu_L(N, M) = E_{CL}, \tag{26}$$
$$\mu_R(N, M+1) - \mu_R(N, M) = E_{CR}, \tag{27}$$
$$\mu_L(N, M+1) - \mu_L(N, M) = \mu_R(N+1, M) - \mu_R(N, M) = E_{Cm}. \tag{28}$$

There is an insightful exercise which consists in studying the expression of the total energy $U(N, M)$ in the limits illustrated in Fig. 11. On the one hand, when the two dots are uncoupled, $C_\mathrm{m} = 0$ and therefore $E_{Cm} = 0$. In this case, the total energy is simply the sum of the energies of the two individual dots, $U(N, M) = U_L(N) + U_R(M)$,

$$U(N, M) = \frac{(-eN + C_\mathrm{gL} V_\mathrm{gL})^2}{2C_\mathrm{L}} + \frac{(-eM + C_\mathrm{gR} V_\mathrm{gR})^2}{2C_\mathrm{R}}, \tag{29}$$

and the charge stability diagram is a rectangular grid (Fig. 11a). On the other hand, when the two dots are strongly coupled, $C_\mathrm{m}/C_{\mathrm{L(R)}} \to 1$. In this limit, the denominator in the expressions of the charging energies Eq. (25) can be written as

$$1 - \frac{C_\mathrm{m}^2}{C_\mathrm{L} C_\mathrm{R}} \approx 1 - \frac{1}{1 + \frac{\tilde{C}_\mathrm{L} + \tilde{C}_\mathrm{R}}{C_\mathrm{m}}} \approx 1 - \left(1 - \frac{\tilde{C}_\mathrm{L} + \tilde{C}_\mathrm{R}}{C_\mathrm{m}} \right) = \frac{\tilde{C}_\mathrm{L} + \tilde{C}_\mathrm{R}}{C_\mathrm{m}}, \tag{30}$$

where we defined $\tilde{C}_\mathrm{L} = C_\mathrm{L} - C_\mathrm{m}$ and $\tilde{C}_\mathrm{R} = C_\mathrm{R} - C_\mathrm{m}$. This leads to

$$E_{CL} \approx E_{CR} \approx E_{Cm} \approx \frac{e^2}{\tilde{C}_\mathrm{L} + \tilde{C}_\mathrm{R}}. \tag{31}$$

Rearranging the terms in Eq. (25) gives

$$U(N, M) = \frac{\left[-e(N + M) + C_\mathrm{gL} V_\mathrm{gL} + C_\mathrm{gR} V_\mathrm{gR} \right]^2}{2\left(\tilde{C}_\mathrm{L} + \tilde{C}_\mathrm{R} \right)}, \tag{32}$$

which is the energy of a single dot with total charge $N + M$ and capacitance $\tilde{C}_\mathrm{L} + \tilde{C}_\mathrm{R}$ (Fig. 11c).

Finally, in the intermediate regime of weak coupling, $C_\mathrm{m} < C_\mathrm{L}, C_\mathrm{R}$ we obtain the well-known honeycomb pattern (Fig. 11b and d).

C Additional information on characterization of the cavity

Raw outputs of Sonnet simulations are shown in Figs. 28 and 29. The magnitude and phase of the transmission coefficient S_{21} are plotted for different combinations of line and turn numbers. The data from Fig. 15 has been extracted from these traces.

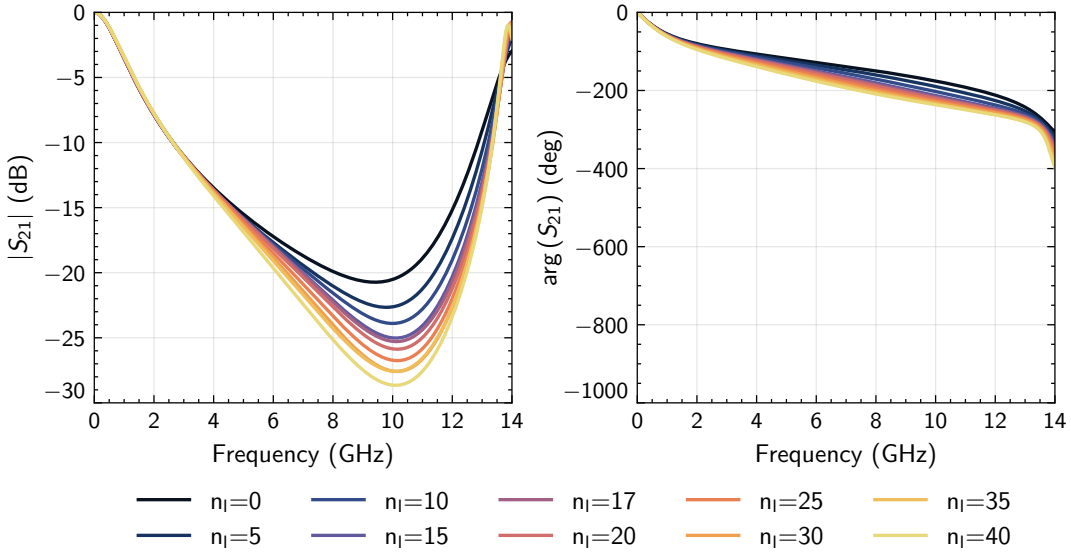

Figure 28: Sonnet simulation outputs for fixed $n_{turns} = 8$ and varying n_{lines}. Compared to Fig. 29, the effect of changing the number of lines is less pronounced.

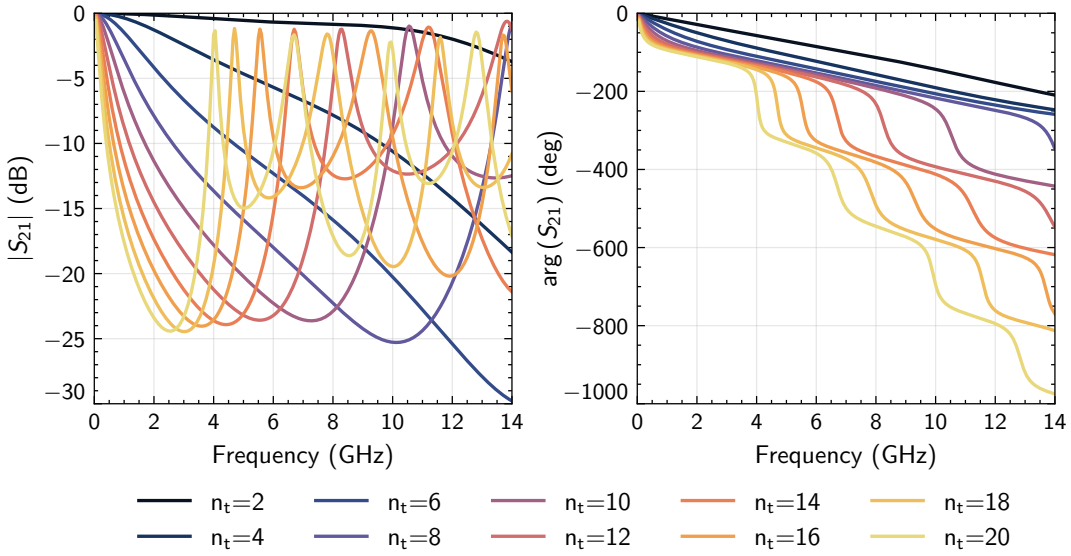

Figure 29: Sonnet simulation outputs for fixed $n_{lines} = 17$ and varying n_{turns}. The magnitude plot shows a mode at high frequencies that is shifted towards lower frequencies when increasing the number of turns. It is responsible for the increasing trend of data in Fig. 15b for $n_t > 12$.

The transmission through the microwave cavity has been also simulated in Sonnet. The comparison of the results and the corresponding experimental measurements are shown in Fig. 30. The agreement is good, even if extra RF components in the dewar as well as chip imperfections add frequency-dependent features to the measured data, *i.e.* wiggles and dips in the transmission.

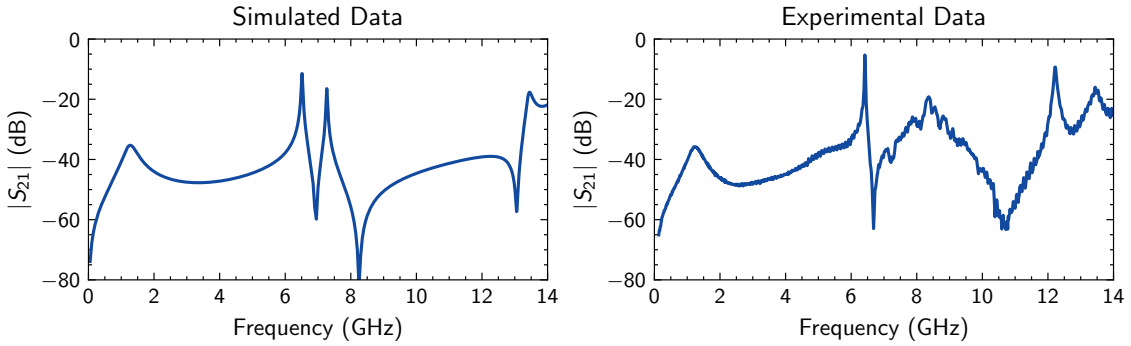

Figure 30: Sonnet simulation of the transmission through the cavity compared to experimental measurements performed in a helium dewar at 4 K. The mode at 6.3 GHz is the cavity resonance.

For the measurements in the helium dewar, the first step is to prepare the chips. The lift-off of a polymethyl methacrylate (PMMA) protective layer is done in acetone and overnight. Then, the chips are rinsed in isopropanol (IPA) and dried with a nitrogen gun. Figures 31a and b show pictures of the clean chips.

Then, chips are glued on a PCB sample holder, as shown in Fig. 31d and e. Next, the chip is wirebonded to the PCB lines, as in Fig. 31f. Note that the chip shown in this picture is different: it only has RF filters, and it is the one used to measure the data in Fig. 16. Apart from making connections to the lines, wirebonds are also used to define properly the ground plane of the chip.

Finally, the PCB is mounted on a RF stick, and secured with aluminum tape, as shown on the left of Fig. 31c. The RF stick is then inserted in the helium dewar, and the measurements are performed connecting the input and output ports of the chip to a vector network analyzer using coaxial cables.

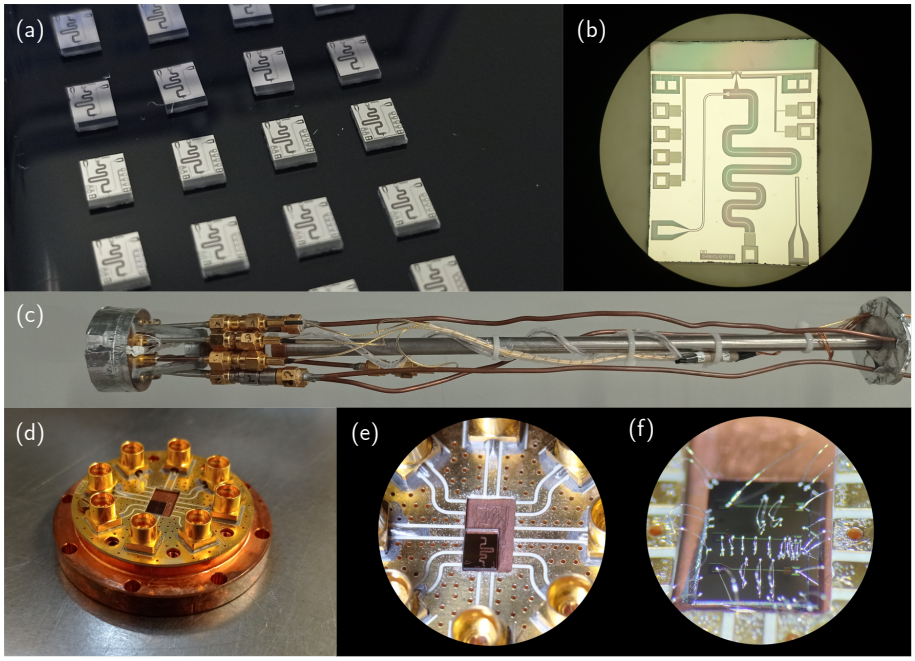

Figure 31: Pictures to illustrate the cooldown procedure. (a) Gel pack where chips are stored after cleaning. (b) Close-up view of a clean chip under the optical microscope. (c) RF stick with a PCB sample holder mounted on it. (d) PCB sample holder. (e) PCB sample holder with chip glued on it. (f) Chip wirebonded to the PCB lines.

D Further insights on resonance fitting

This appendix summarizes the method used to extract the resonance frequency and quality factors from complex VNA data. The main text presents the ideal expression of the reflection coefficient S_{11} to explain the physics, but all data fitting in this thesis is performed with NLQFIT 7 [31, 32]. The key idea is to fit the complex data directly with a model that absorbs common measurement non-idealities such as cable delay, impedance mismatch, and slow frequency-dependent gain. This improves robustness and yields reliable f_r, Q_l, Q_i, Q_e. The fitted model for the measured data is

$$S_a(f) = \alpha(f)\, e^{-i\phi}\, e^{-i\,\Delta\phi(f)} \left[S_D + \frac{d\, e^{i\theta}}{1 + iQ_l\, t(f)} \right], \qquad t(f) = \frac{2(f - f_r)}{f_r}, \tag{33}$$

where f_r and Q_l are the resonance frequency and loaded quality factor. The bracketed term is the usual Q-circle. The prefactors account for the measurement chain: $\alpha(f)$ represents a slowly varying amplitude correction that captures background gain; ϕ is a static phase offset; $\Delta\phi(f)$ is a slowly varying phase term; S_D sets the off-resonance point in the complex plane and allows the circle center to be shifted from the origin; d controls the circle diameter; and θ is a rotation angle. From the fitted parameters one obtains f_r and Q_l directly; the internal and external quality factors follow from $Q_l^{-1} = Q_i^{-1} + Q_e^{-1}$ and the coupling coefficient β that can be extracted from the Q-circle diameter.

In relation to the ideal expression quoted in the main text, which assumes perfect matching and negligible backgrounds, this model differs by allowing frequency-dependent amplitude and phase corrections and the circle to be shifted and rotated in the complex plane. When these corrections are negligible the fitted model reduces to the ideal form used for explanation in the main text, but in general the augmented model provides better fits to real laboratory data.

For the numerical optimization, NLQFIT 7 minimizes residuals in the complex domain using the compact parameterization

$$r_i = S_i - \left[m_1 + im_2 + (m_3 + im_4)\, y_i \right] \exp\left(im_7\, \tfrac{f_i - f_r}{f_{\mathrm{lwst}}} \right), \tag{34}$$

with

$$y_i = \frac{1}{1 + iQ_l\, t_i}, \quad t_i = 2\tfrac{f_i - f_r}{f_r}. \tag{35}$$

Here (m_1, m_2) encode a complex offset that captures background transmission or reflection, (m_3, m_4) scale and rotate the Q-circle contribution y_i, and m_7 captures a linear phase slope with frequency that effectively models cable delay. This formulation ensures that magnitude and phase are treated consistently by fitting the real and imaginary parts together. The equivalence between Eqs. (33) and (34) can be found in Refs. [31, 32].

In practice this approach is advantageous because it provides reliable fits even when the resonance is weak or distorted by the measurement chain. The Python implementation used in this thesis provides a graphical interface for selecting files and the frequency band of interest, applies an optional baseline correction, and then performs the NLQFIT 7 optimization to return (f_r, Q_l, Q_i, Q_e).

Note: The code is available at github.com/BeBerasategi/Resonance-fitting.